



**LUND**  
UNIVERSITY

Master of  
Science Thesis  
VT2015

# Semi-automatic evaluation of lymph nodes in patients with rectal neoplasms with diffusion weighted MRI

---

Daniel Roth

## Supervision

Sven Månsson, Peter Leander and Lisa Hörberg, Malmö

This work has been performed at  
Medical Radiation Physics, Department of Translational Medicine,  
Skåne University Hospital, Malmö

Department of Medical Radiation Physics,  
Clinical Sciences, Lund  
Lund University

---

## Abstract

### Background and purpose

Several studies have shown that surgery with pre- or post-operative adjuvant radiotherapy reduces the local recurrence rate in rectal cancer patients. Preoperative evaluation of lymph node involvement is difficult but important for assessing the benefit of radiotherapy. Radiologists usually assess lymph node sizes and shapes to determine nodal involvement, but it can be difficult to distinguish between normal and involved nodes. Apparent diffusion coefficients (ADC) of lymph nodes obtained from diffusion weighted MRI (DWI) can also be used when estimating nodal involvement, with malignant nodes tending to have more impeded diffusion.

Manual assessment and delineation of lymph nodes is error prone, may be subject to inter- and intra-observer variability and may be time-consuming. The use of a semi-automatic segmentation techniques can reduce inter- and intra-observer variability and give a more exact segmentation in a shorter time. There is however no segmentation technique that works well in all situations. The purpose of this work was to evaluate several techniques and develop a program for semi-automatic 3D segmentation of lymph nodes in diffusion weighted MR images and evaluation of lymph node sizes and ADC values.

### Materials and methods

A program for evaluation of different 2D segmentation techniques on lymph nodes was written in MATLAB. The segmentation techniques were evaluated on lymph nodes in whole body DWI images acquired on a 1.5 T MRI scanner. Thereafter, a program was developed for segmentation of lymph nodes in three dimensions. The program used a 3D spiral scanning technique to transform image intensities in the 3D images into a 2D image. The surface of the lymph node was then identified in the transformed 2D image using an active contour-like iterative algorithm. The surface was then transformed back into a volume of interest (VOI) in the 3D data. The resulting VOIs were used to extract mean ADC values and volumes of the lymph nodes. Finally, two radiologists used the program to delineate pelvic lymph nodes in 4 patients before and after neo-adjuvant chemoradiotherapy.

### Results

A total of 35 lymph nodes were marked by the radiologists and 32 of these were successfully delineated by the program. The total volume of all lymph nodes was 12.1 mL before and 9.96 mL after treatment. The average reduction in volume per lymph node was 100  $\mu$ L, not significantly different from zero, ( $p = 0.065$ ). The average ADC decreased with  $99 \times 10^{-6} \text{ mm}^2 \text{ s}^{-1}$ , not significantly different from zero, ( $p = 0.084$ ).

### Conclusions

Preliminary results indicated that the 3D spiral scanning algorithm is capable of 3D segmentation of lymph nodes in the abdomen. Data obtained by radiologists when testing the primary program indicated that lymph node volumes and ADC values decrease after chemoradiotherapy, although more patients are required to draw a definite conclusion.

---

## Populärvetenskaplig sammanfattning

Efter prostatacancer, bröstcancer och hudcancer är cancer i tjocktarm och ändtarm tillsammans den fjärde vanligaste typen av cancer i Sverige med omkring 11% av alla cancerfall. Förekomsten av tjock- och ändtarmscancer varierar i världen och den högsta förekomsten av denna välfärdssjukdom finns i USA, Europa, Australien och Nya Zeeland. De lägsta incidenserna finns i utvecklingsländerna. Relativt få unga drabbas av tjock- och ändtarmscancer. Av de som drabbas är 75% över 65 år och enbart 5% under 50 år. Ungefär lika många män som kvinnor drabbas av tjocktarmscancer och vid ändtarmscancer drabbas män något mer än kvinnor.

Cancer i tjocktarm och ändtarm behandlas huvudsakligen med kirurgi. Inför kirurgi görs en bedömning om all tumör kan avlägsnas eller om det finns risk för att delar av canceren blir kvar i kroppen. Om all cancer inte kan avlägsnas med enbart kirurgi kan man strålbehandla tumören för att senare avlägsna all cancer med kirurgi. Vid tidig diagnos av canceren brukar risken att cancer ska finnas kvar i kroppen efter kirurgi vara så liten att förbehandling med strålbehandling är en onödig överbehandling. Vid en mera avancerad cancer kan en kort strålbehandling inför kirurgi vara önskvärd då studier har visat att detta leder till en minskad andel canceråterfall. Vid bedömningen av cancerens omfattning ser man på hur tumören har växt, om cancer har spridit sig till lymfkörtlar, samt om det finns avlägsna metastaser. Genom att bedöma cancerens stadium i dessa tre aspekter tillsammans med ytterligare faktorer kan man avgöra hur canceren optimalt behandlas. När det gäller tumören fungerar de metoder som finns idag bra, men för att bedöma om canceren har spridit sig till lymfkörtlar så behövs bättre metoder. I nuläget bedöms lymfkörtlar genom att radiologer granskar snittbilder av lymfkörtlarna tagna med exempelvis en magnetkamera. Vid bedömningen av lymfkörtlarna används kriterier såsom storlek och form för att avgöra om cancer har spridit sig till dem. Problemet med en sådan bedömning är att det kan vara svårt att skilja lymfkörtlar som förstörats på grund av cancer från lymfkörtlar som förstörats av inflammation. Ett möjligt alternativ för att granska lymfkörtlar är att avbilda vattenmolekylernas rörelsefrihet i kroppen med hjälp av en magnetkamera. I sådana bilder tenderar lymfkörtlar med cancer att ha en lägre rörelsefrihet för vattenmolekylerna än friska lymfkörtlar. För att mäta vattenmolekylernas rörelsefrihet i lymfkörtlarna behöver de ritas ut i bilderna, vilket innebär att de pixlar som tillhör lymfkörtlarna i bilderna måste anges. Att rita ut lymfkörtlar för hand är emellertid tidskrävande, särskilt om lymfkörtlarna syns i flera snittbilder, och det som ritats ut varierar beroende på personen som ritat. Ett alternativ till att rita och bedöma lymfkörtlar för hand är att låta ett datorprogram rita ut lymfkörtlarna. Ett sådant program kan rita ut lymfkörtlar som syns i flera snittbilder snabbt och det som ritats ut beror inte på personen som använder programmet.

I detta examensarbete testades många olika algoritmer för att automatiskt rita ut lymfkörtlar. Ett datorprogram baserat på den bästa algoritmen utvecklades sedan för att rita ut lymfkörtlar och mäta storlek och vattnets rörelsefrihet. Tanken är att detta program senare ska användas i en klinisk studie för att undersöka om storlek på lymfkörtlar och rörelsefrihet hos vattenmolekyler kan användas för att avgöra om körtlarna innehåller cancerceller.

---

## Abbreviations

- DWI – Diffusion weighted MRI
- ADC – Apparent diffusion coefficient
- TME – Total mesorectal excision
- VOI – Volume of interest
- ROI – Region of interest

---

# Contents

<b>Abstract</b>	<b>1</b>
<b>Popular science summary</b>	<b>2</b>
<b>Abbreviations</b>	<b>3</b>
<b>1 Introduction</b>	<b>6</b>
<b>2 Aim</b>	<b>7</b>
<b>3 Theory</b>	<b>8</b>
3.1 Image segmentation . . . . .	8
3.2 Thresholding . . . . .	8
3.3 Region growing . . . . .	8
3.4 Edge detection . . . . .	9
3.5 Segmentation by 3D spiral scanning . . . . .	9
3.6 Deformable models . . . . .	15
3.7 Fast marching method . . . . .	15
<b>4 Materials and methods</b>	<b>16</b>
4.1 Image acquisition . . . . .	16
4.2 Evaluation of segmentation techniques . . . . .	17
4.2.1 Region growing . . . . .	19
4.2.2 Edge detection . . . . .	21
4.2.3 Thresholding . . . . .	22
4.2.4 Fast marching method . . . . .	23
4.2.5 2D ('spiral') scanning algorithm . . . . .	24
4.2.6 Active contour algorithm . . . . .	31
4.3 Development of primary program . . . . .	31
4.3.1 Segmentation algorithm . . . . .	31
4.3.2 Initial evaluation of the segmentation algorithm . . . . .	35
4.4 Evaluation of primary program by radiologists . . . . .	36

---

<b>5</b>	<b>Results</b>	<b>37</b>
5.1	Evaluation of segmentation techniques . . . . .	37
5.1.1	Region Growing . . . . .	37
5.1.2	Edge Detection . . . . .	38
5.1.3	Thresholding . . . . .	39
5.1.4	Fast marching method . . . . .	41
5.1.5	2D scanning algorithm . . . . .	41
5.1.6	Active contour algorithm . . . . .	45
5.2	3D spiral scanning segmentation results . . . . .	46
5.3	Evaluation of primary program by radiologists . . . . .	48
<b>6</b>	<b>Discussion</b>	<b>55</b>
<b>7</b>	<b>Conclusions</b>	<b>60</b>
<b>8</b>	<b>References</b>	<b>61</b>

---

# 1 Introduction

Colorectal cancer is the fourth most common cancer and constitutes around 11% of all cases in Sweden [1]. The disease is relatively uncommon in young individuals and around 75% of all cases occur after 65 years of age [2]. The primary treatment of colorectal cancer is surgery. For rectal cancer, a standardized surgical technique is the total mesorectal excision (TME) in which the mesorectal compartment, which consists of the rectum and the surrounding fat, is removed. The primary treatment may also include neo-adjuvant (pre-operative) as well as adjuvant (post-operative) chemo- and radiotherapy depending on the stage of the disease [2, 3].

For early cancers where the risk of local recurrence is assessed as low, radiotherapy is deemed as overtreatment. In more advanced cancers neo-adjuvant treatment reduces the probability of local recurrence [2, 3]. When a treatment strategy using preoperative chemo- and radiotherapy is planned to be used, it is therefore paramount to correctly distinguish preoperatively between the groups that have low and high probabilities of recurrence to find those patients that benefit from the neo-adjuvant treatment. For tumour staging (T-stage), ultrasound and MRI allow accurate assessment of rectal wall layer integrity in superficial rectal cancers. However, identification of nodal metastasis (N-stage) is still a problem for radiologists [3]. For planning of post-operative chemo- and radiotherapy the operated tumour is assessed histologically. With the standard TME surgery, perirectal lymph nodes are also removed and can be assessed, but lateral iliac lymph nodes are normally left behind. There is therefore an increased probability of recurrence in rectal cancers where these nodes are involved. Lateral lymph nodes are therefore subject to correct diagnosis in the preoperative work-up of the patient for planning of adjuvant treatment [3].

For lymph nodes, radiologists may use size and shape criteria to estimate nodal involvement [3, 4]. The problem with the morphological criteria is that it is hard to distinguish metastatic nodes from reactive nodes and micrometastases can be missed in small nodes. There is also a high frequency of normal sized nodes with metastases [3]. Apparent diffusion coefficients of lymph nodes obtained from diffusion weighted (DWI) sequences can also be used when estimating nodal involvement, with malignant nodes tending to have more impeded diffusion [5, 6].

At present, lymph node sizes are commonly assessed manually, which is error prone and may be subject to inter- and intra-observer variability [7, 8]. Several semi-automatic segmentation techniques have been developed to achieve more exact segmentations and measurements of lymph nodes [7]. Semi-automatic segmentation algorithms based on a 3D-spiral scanning algorithm, in which a user independent computer program segments an object designated by a user, have been successfully used in many applications to reduce inter- and intra-observer variability and improve measurement precision compared to manual delineation [7, 8, 9]. An advantage of the 3D-spiral scanning technique is that it simplifies segmentation of 3D objects by transforming their image intensities into 2D images [10].

---

## 2 Aim

The purpose of this work was to develop a program for semi-automatic segmentation of lymph nodes in diffusion weighted magnetic resonance images (DWI) and to evaluate them with respect to volume and apparent diffusion coefficients (ADC). These parameters were then planned to be paired in the future with histology data in a clinical study to investigate if volume and a histogram analysis of the ADC values could be used as a parameter for determining if lymph node contains cancerous cells.



---

## 3 Theory

### 3.1 Image segmentation

Image segmentation is the process in which an image is divided into regions of pixels which are similar in terms of some characteristic or feature [11]. Segmentation is an important tool in medical imaging for extracting information from images to help clinicians evaluate structures, diseases and the need for surgery or radiotherapy. There is a large number of applications for segmentation in medical imaging and each field offers different challenges in terms of noise, contrast and occlusion from structures. Many segmentation techniques have been developed to deal with these challenges. However, there is no single technique that works well in all applications. The technique used may depend on the goal of the segmentation and the assumed properties of the images [11, 12].

Several techniques for image segmentation are discussed in the following sections. Section 3.2, 3.3 and 3.4 are described in the e-book *Handbook of Medical Imaging* by Bankman, I N (2000) [11].

### 3.2 Thresholding

Thresholding is a common segmentation technique in which pixels in an image are divided into groups having values greater than or less than a threshold. One or more thresholds may be used in this technique. If one threshold is used for the entire image, the thresholding is called global. If the original image is called  $f(x, y)$  and  $T$  is the threshold value, then the globally thresholded image, called  $g(x, y)$ , is defined as:

$$g(x, y) = \begin{cases} 1 & \text{if } f(x, y) > T \\ 0 & \text{if } f(x, y) \leq T \end{cases} \quad (1)$$

The result of the thresholding is the binary image  $g(x, y)$  whose pixels have a value of 1 for objects in the image  $f(x, y)$  and a value of 0 for the background in the image  $f(x, y)$ .

There are many methods for choosing a threshold. Examples of methods include histogram based methods that separates an object from the background by choosing a threshold between two peaks in a bimodal histogram, and classification models which attempts to minimize the number of object pixels misclassified as background and background pixels misclassified as object.

### 3.3 Region growing

The region grow technique works by finding connected groups of pixels that are similar in terms of some criteria. The growing is initiated with a pixel or a group of pixels called seeds. The seeds can be provided by an operator or an automatic procedure. After initiating, the method examines pixels

---

that neighbour the region. The pixels that passes the homogeneity criterion of the method are added to the region. This step is repeated until no new pixels are added to the region. The object in the image is then composed of the pixels that were accepted during the growing process.

There are many possible homogeneity criteria. One example is to compare the value of a neighbouring pixel with the mean value of the region and include the neighbour if the difference is below a specified value. The choice of this criterion will have a large effect on the resulting region. A non-optimal choice may cause the region to grow out into the background and include unwanted pixels. The result may also depend on the starting point. An advantage of this method is that it produces connected regions.

### 3.4 Edge detection

Edges of objects on an image are related to the image intensity gradient  $\vec{G}$ , which is the derivative of the image  $f(x, y)$ . The gradient magnitude can be calculated as:

$$|\vec{G}| = \sqrt{G_x^2 + G_y^2} = \sqrt{\left(\frac{\partial f}{\partial x}\right)^2 + \left(\frac{\partial f}{\partial y}\right)^2} \quad (2)$$

where  $G_x$  and  $G_y$  are the gradients in the x and y-direction respectively. In discrete images where continuous derivation is not possible,  $G_x$  and  $G_y$  are often replaced with differentiations and/or convolutions. For example, in a Sobel edge operator  $G_x$  and  $G_y$  may be approximately calculated by convolving  $f(x, y)$  with the kernels

$$\begin{bmatrix} -1 & 0 & 1 \\ -2 & 0 & 2 \\ -1 & 0 & 1 \end{bmatrix} \text{ and } \begin{bmatrix} -1 & -2 & -1 \\ 0 & 0 & 0 \\ 1 & 2 & 1 \end{bmatrix}$$

respectively. The gradient magnitude can then be calculated with equation 2.

In many methods, the calculation of the gradient magnitude is followed by a thresholding operation to identify edges in the image. However, selecting a threshold may be a difficult task and a common problem is that edges do not fully surround objects in the image. Solutions to this problem may involve a post-processing step where edges belonging to the same boundary are linked together. Such solutions can be unreliable however.

### 3.5 Segmentation by 3D spiral scanning

3D spiral scanning is a technique developed by Jiahui Wang, Roger Engelmann, and Qiang Li [10] that can simplify segmentation of objects in 3-dimensional data. With this technique, sampling is

made from the data along radial lines originating from the center of the object. Each radial line is defined by an azimuth angle and an elevation angle. The definition of azimuth angles and elevation angles in this section are based on the definitions used by Wang, J et al. with minor modifications. In the article by Wang, J et al. an elevation angle of 0 corresponds to a direction upwards towards the "north pole" and an elevation angle of  $\pi$  correspond to a direction towards the "south pole" with no provided equation for transforming the angles to Cartesian coordinates. In this section and all following sections, the azimuth angle  $\alpha$  lies in the range  $[0, 2\pi]$  and the elevation angle  $\beta$  lies in the range  $[-\frac{\pi}{2}, \frac{\pi}{2}]$ , with  $\beta = -\frac{\pi}{2}$  corresponding to the "south pole" and  $\beta = \frac{\pi}{2}$  corresponding to the "north pole". This definition follows the notation used by MATLAB functions and is shown in figure 1. By defining the azimuth angle and elevation angle according to equation 3, the radial lines are generated in a sequential order.

$$\begin{aligned}
 k &= 1, 2, 3, \dots, 2N^2 \\
 \alpha_k &= \frac{k \cdot \pi}{N} \\
 \beta_k &= \frac{k \cdot \pi}{2 \cdot N^2} - \frac{\pi}{2}
 \end{aligned} \tag{3}$$

Here,  $N$  is the number of revolutions used in the spiral scanning and  $2N^2$  is the total number of radial lines.

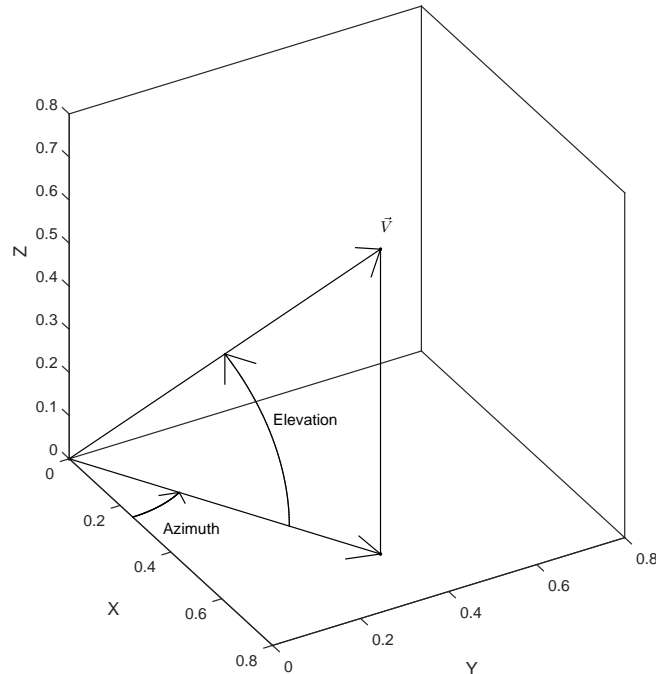


Figure 1: Conversion from azimuth angle and elevation angle to a direction in Cartesian coordinates.

The resulting radial line directions generated by equation 3 with  $N = 15$  are shown in figure 2. The directions  $\vec{V}_k = (X, Y, Z)$  shown in figure 2 have been calculated with equation 4 with  $r = 1$ .

$$\begin{aligned} X &= r \cdot \cos(\beta_k) \cdot \cos(\alpha_k) \\ Y &= r \cdot \cos(\beta_k) \cdot \sin(\alpha_k) \\ Z &= r \cdot \sin(\beta_k) \end{aligned} \quad (4)$$

The generation of one radial line from an azimuth and elevation angle is shown in figure 1.

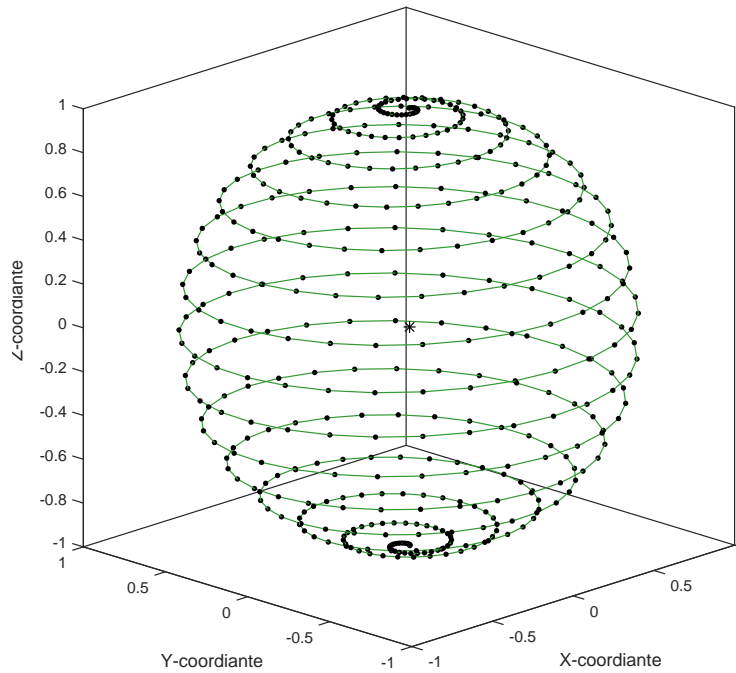


Figure 2: Radial line directions generated with equation 3. The radial line directions are indicated by dots. The lines connecting the dots indicates the sequential order. The sampling origin is indicated by a star.

With equation 3 and 4, the sampling starts at the "south pole" and ends at the "north pole". The advantage of equation 3 is that the radial lines appear in a sequential order. However, the radial lines are not distributed evenly; there are more lines around the poles than around the equator. This is a disadvantage according to Wang et al. although the reason why is not specified. The authors solved this by choosing the number of points for each rotation based on the circumference of the circle at the elevation angle  $\beta$ . Their result was that  $2N \cdot \sin(\beta + \frac{\pi}{2})$  points should be used on the rotation at elevation  $\beta$  to achieve evenly distributed points.

The sample direction distributions investigated by Wang et al. are shown in figure 3 (a–c). Figure 3 (a) illustrates a non-sequential ordering of the sample directions which is incompatible the segmentation technique used by the authors. Figure 3 (b) illustrates the sequential ordering of sample directions

described by equation 3. Figure 3 (c) illustrates the distribution where the sample directions are evenly distributed spatially. The authors obtained slightly better segmentation results when using the sampling technique shown in figure 3 (c) compared to the technique in figure 3 (b). In this work, the sample direction distribution shown in figure 3 (b) is used because of the more basic definition of azimuth and elevation angles and the simpler identification of neighbouring radial lines in the latitude direction.

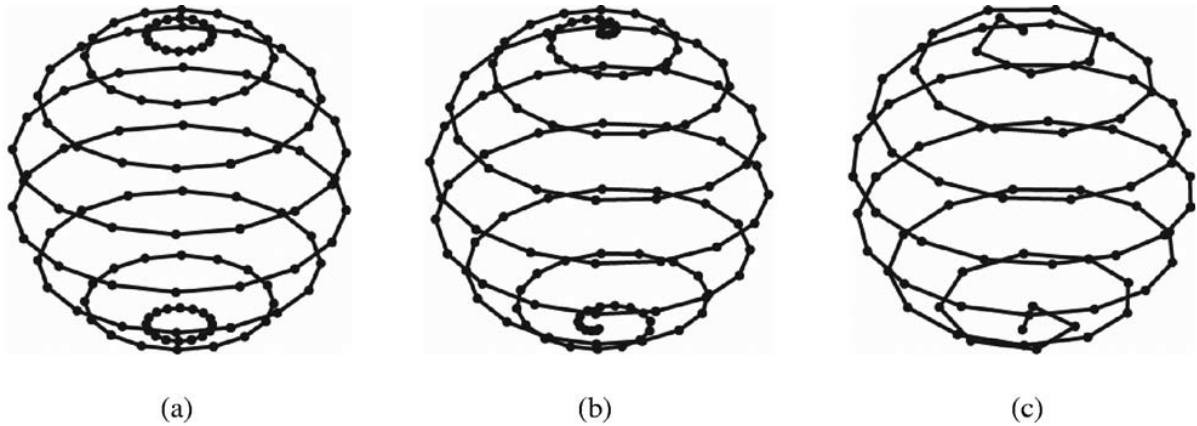


Figure 3: Sample directions with (a) even partition of azimuth and elevation angles, (b) even partition of azimuth and elevation angles in a sequential order and (c) even spatial distribution of radial lines. [Wang, J et al. 2007 Fig.2 p.4680[10]]

Once a set of radial line directions has been obtained, samples of the image intensities are made along the radial lines. A cubic interpolation method is used in this work to sample the image intensities, since the radial lines doesn't intersect voxel centres exactly. The technique used by Wang et al. for the sampling is not specified. The sampled points can then be arranged in a 2D array or image where each column represents samples along one radial line and the ordering of the columns follows the sequential order of the radial lines. This arrangement of the sample points is denoted as the two-dimensional  $k$ - $r$ -space, where  $k$  indicates the sequential ordering of the radial lines and  $r$  indicates the distance of the sample point from the origin. Figure 5 shows an example of this ordering for a sampling of the synthetic image shown in figure 4. The image intensity in figure 5 corresponds to image intensity in figure 4. The points in figure 5 have been sampled along radial lines generated with equation 3 with  $k = 1, 3, 5, \dots, 2N^2$  and  $N = 100$ , i.e. with 10000 lines. Only the sample points for the first 2000 radial lines are shown.

After the spiral sampling transformation, a surface of an object in the 3-dimensional data becomes a line in the 2-dimensional image, which simplifies the segmentation. For segmentation in the 2D image, Jiahui Wang et al. used a dynamic programming algorithm, which is a technique for solving optimization problems in a multiple decision process, to find an optimal path through the image. An example of a path through an image is shown in figure 6. To find the most optimal path among the

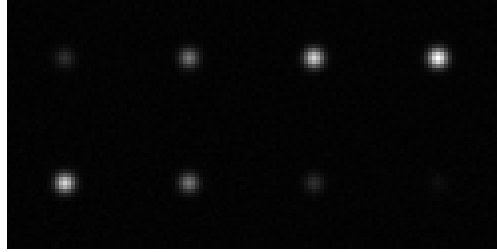


Figure 4: Montage of 8 slices from a synthetic image.

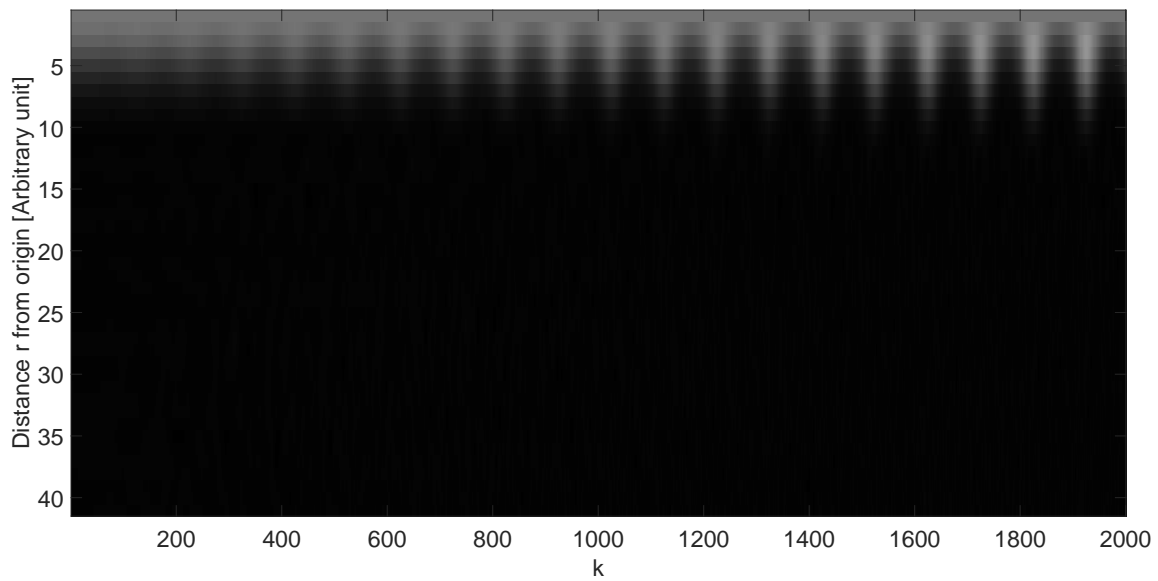


Figure 5: Points sampled along radial lines. The uppermost row contains samples with a distance of 0 pixels from the sampling origin and the bottommost row contains samples with a distance of 20 pixels from the origin. The leftmost columns corresponds to radial lines near the "south pole".

large set of possible paths through the image, the authors gave each possible path a 'cost' based on its characteristics such as how smooth it was and how well it followed contours in the image. The most optimal path was then obtained by using the dynamic programming algorithm to find the path with the smallest possible cost.

The authors assigned costs to each pixel in the 2D image based on the vertical image gradient where a large image gradient was assigned a large (in absolute value) negative cost. The cost based on the image gradient was used as an external cost for the path. An internal cost for the path was also used based on the smoothness of the resulting surface. The internal cost used differences in  $y$ -coordinates of nearby points on the path as a cost based on smoothness. This meant that a relatively smooth object surface yielded a low cost whereas a bumpy surface yielded a larger cost. Differences in  $y$ -coordinates were formed both in the longitude direction (between  $i$ :th and  $i - 1$ :th points) and in the latitude direction. Using these costs, a dynamic programming algorithm was used to find the most optimal path that yielded the lowest cumulative cost through the 2D image. An example of a path through a 2D image, acquired with an algorithm developed in this work is shown in figure 6.

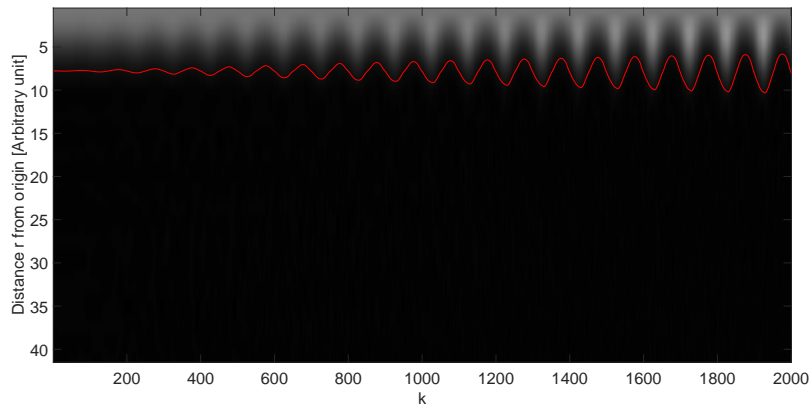


Figure 6: Example of a path through the 2D image shown in figure 5.

After the segmentation in the  $k$ - $r$ -space, the path through the image will contain a set of radii, each associated with a pair of azimuth and elevation angles. Jiahui Wang et al. used this to project back a set of points into 3D-space set and obtained a sparse point cloud. The authors then used these points to determine which voxels were inside the object of interest by calculating "virtual" radial lines between the voxels in the 3D data set and the center of the volume of interest (VOI). These virtual radial lines were then compared to real nearby radial lines. If the distance between a voxel and the center of the VOI was less than the mean of the radii associated with the nearby radial lines, then the voxel was included in the VOI.

This scanning technique has been used to segment various objects such as pulmonary nodules in CT images [10], lymph nodes in thoracic CT images [7], liver tumours in CT images [8], breasts in MR images [13] and brain tumours in MR images [9].

---

### 3.6 Deformable models

Active contours were introduced by Kass M, Witkin A, and Terzopoulos D in 1987 [14]. The active contours, also called snakes, are guided by external and internal energies and forces that pull them towards structures of interest such as object edges or lines as they minimize their total energies. They cannot locate and segment an object all on their own and require another algorithm or a user to place them near an object of interest. Once placed, the contours move across the image to minimize their total energy. The internal energy serves to make the contours smooth or piecewise smooth. The external energy pushes the contours towards image features of interest. What the contour is attracted to depends on how the external energy is defined. By defining the external energy  $E$  as:

$$E = w \cdot f(x, y) \quad (5)$$

where  $w$  is a weight factor and  $f(x, y)$  is the image intensity, one obtains a snake that is attracted to bright or dark lines in the image, depending on the sign of  $w$ . By defining the external energy as the gradient of the image intensity:

$$E = -|\nabla f(x, y)|^2 \quad (6)$$

one obtains a snake that is attracted to sharp contours in an image. By using other external energies or linear combinations of external energies, different snake behaviours can be created.

### 3.7 Fast marching method

The fast marching method is a technique for tracking surfaces that are monotonically growing with a speed that only depends on position. The method has the ability to track fronts that develop corners, cusps, break apart, and merges [15, 16]. The surface can be compared to the edge of an acid that is corroding its way into an exterior region with the speed at which various parts of the surface is moving being dependent on the properties of the materials in the exterior region [17]. Such a surface is shown in figure 7. The method can be used to segment images by, for example, initiating the surface inside an object and make the surface expand slowly when it encounters strong gradients between the object of interest and the background in the image.

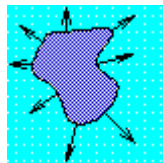


Figure 7: Dark blue inside expanding into a light blue outside. A black contour tracked in this method separates the two regions. [Sethian, J.A c. 2006 [17]]



---

## 4 Materials and methods

To test and evaluate different segmentation techniques, a user interface was constructed in MATLAB R2014b. This program, referred to as the segmentation evaluation program, could read pixel data from DICOM files, select and display single slices from the data, and extract histogram data from a selected region and was used for evaluation of segmentation techniques in single slices of diffusion weighted MR images of the abdomen. The segmentation evaluation program could also generate a synthetic image with Rician distributed noise. This image was briefly used for the initial development of segmentation techniques before the ability to read and display images from DICOM files were added. A second user interface, referred to as the primary program, utilizing a selected segmentation technique from the previous program was then developed for handling multislice images, segmenting multislice data and extracting useful data on lymph nodes.

### 4.1 Image acquisition

Most DWI images used for evaluation of the segmentation algorithms were acquired on a 1.5 T MR imager (Avanto Fit, Siemens Healthcare, Erlangen, Germany). Typical MR sequence parameters are shown in table 1. Some images were acquired with similar protocols on a 3 T Siemens Trio. The set of diffusion weighted images with the highest b-value was used for evaluation of segmentation techniques.

Table 1: Acquisition parameters.

Sequence type	DWI 2D spin echo EPI
TR/TE	4600/62 ms
b-values	50, 400, 800 $\text{s cm}^{-2}$
Number of averages	4, 7, 14 (for b-values 50, 400, 800)
FOV	$300 \times 116$ (read $\times$ phase) $\text{mm}^2$
Number of slices	30
Slice orientation	Transverse
Slice thickness and gap	5 mm, 1 mm gap
Acquisition matrix	$128 \times 110$ (read $\times$ phase)
Parallel imaging settings	GRAPPA, acceleration factor 2
Acquisition time	6 min 10 s

The MR scanner also calculated apparent diffusion (ADC) maps using the images obtained with the three b-values. These maps were used in the primary program.

---

## 4.2 Evaluation of segmentation techniques

The segmentation evaluation program provided a set of tools, including:

- A crosshair for specifying starting pixel(s) for segmentation techniques requiring initial seeds.
- An edit box for selecting a threshold for segmentation techniques requiring this.
- An edit box for specifying a region size for techniques that measures local properties.
- A list of actions for preprocessing and segmenting the displayed image.

The purpose of this program was to evaluate segmentation techniques and identify the one most suitable for implementation in the final user interface with added 3-dimensional segmentation capabilities. Screenshots of the program are shown in figures 8 and 9.

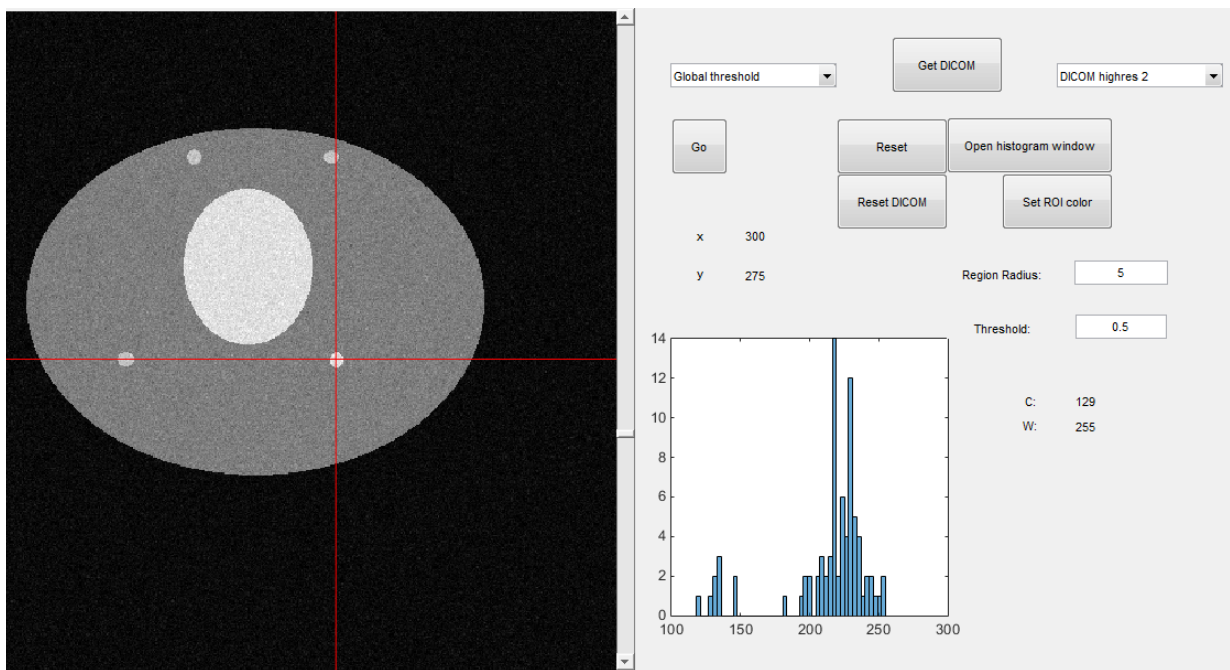


Figure 8: Screenshot of the segmentation evaluation program. A synthetic image with Rician distributed noise is shown on the left side of the program window. A histogram of the pixel intensities in a small region of interest is shown in the central axis.

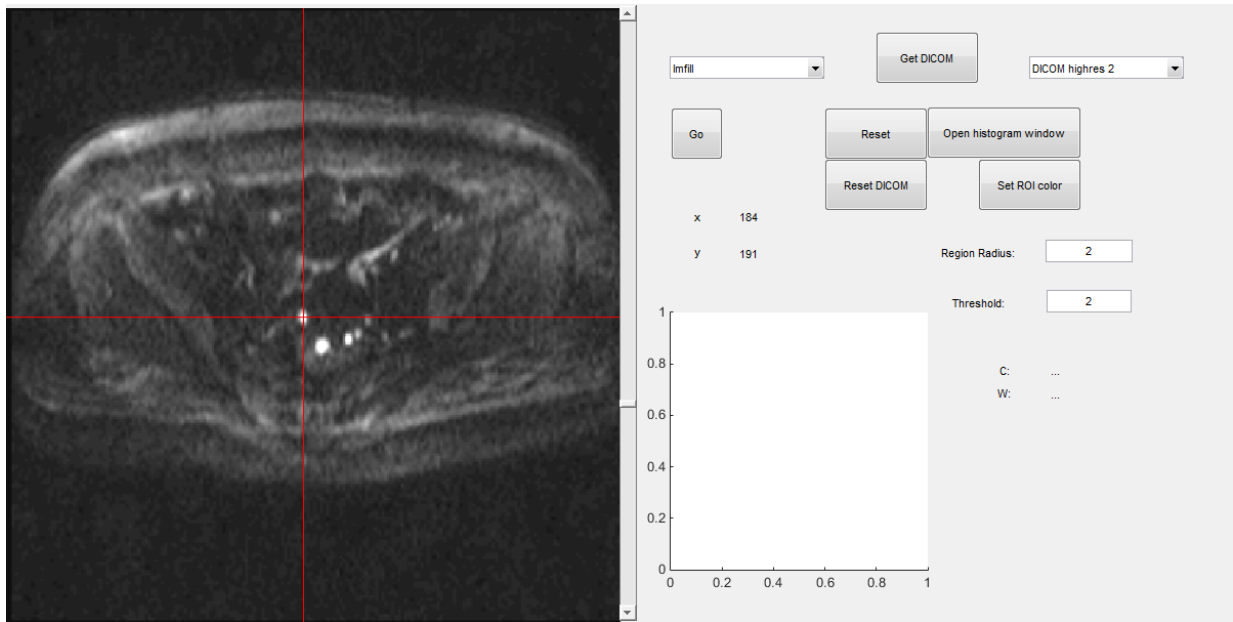


Figure 9: Screenshot of the segmentation evaluation program with DWI data loaded.

The following actions were available to the user:

1. Segment image with a region growing algorithm with various homogeneity criteria
2. Segment image with an active contour algorithm from a MATLAB toolbox
3. Segment image with a fast marching method algorithm from a MATLAB toolbox
4. Segment image with thresholding algorithms
5. Segment image with edge detection algorithms
6. Segment image with 2D ('spiral') scanning algorithms
7. Fill holes in the shown image with a function from a MATLAB toolbox
8. Convolve image with a nine-point-smoothing kernel
9. Convolve image with differentiating kernels

The implemented 2D segmentation techniques were evaluated with respect to:

- Ability to separate a single selected lymph node from background and nearby lymph nodes
- Ability to segment lymph nodes with varying sizes, shapes, signal strengths and background structures without the need for adjusting segmentation algorithm parameters such as thresholds or weight factors

The techniques were also used on more elongated objects, such as nerves, visible in the diffusion weighted images to examine how they performed on shapes differing from the circular or slightly

elliptical lymph nodes. The performances of the techniques on nerves was not factored in when selecting the most suitable method for 3 dimensional lymph node segmentation, but the effects of more non-circular shapes were noted.

The evaluated techniques can segment objects in 2 dimensional images and can be expanded to work in 3 dimensional images. However, the expansion from 2 to 3 dimensions may not be trivial [10].

#### 4.2.1 Region growing

Multiple region growing algorithms were developed and evaluated. The algorithms had the following homogeneity criteria:

1. A neighbouring pixel is included if its intensity  $I$  satisfies the inequality  $|I - M| \leq T$  where  $M$  is the mean value of the initial seed and  $T \in [0, I_{\max}]$  is a threshold selected by the user
2. A neighbouring pixel is included if it satisfies one of the following conditions
  - (a)  $I \geq T \cdot M$  where  $M$  is the mean intensity of the 7 strongest pixels within a radius of  $r$  pixels from the initial seed center,  $T \in [0, 1]$  is a threshold value and  $I$  the pixel intensity
  - (b)  $\frac{D_1}{D_2} \geq T_{\text{Deriv}}$  where  $D_1$  is the image derivative at the examined pixel in the direction inwards towards the starting seed and  $D_2$  the mean slope between the examined pixel and the starting seed and  $T_{\text{Deriv}} \in [0, \infty)$  is a threshold value
3. A neighbouring pixel is first included if it satisfies the condition
  - (a)  $I \geq M_1 \cdot T + M_2 \cdot (1 - T)$  where  $I$  is the pixel intensity,  $M_1$  is the mean of the 7 strongest pixels in the local area,  $M_2$  is the mean of the 16 weakest pixels in the local area, and  $T \in [0, 1]$  is a threshold value. The local area is defined as the region within a radius of  $r_1$  pixels from the initial seed center

Once no neighbours satisfies this criterion, the following criterion is used

- (b)  $\frac{D}{D_{\max}} \geq T_{\text{Deriv}}$  where  $D_{\max}$  is the mean gradient magnitude of the 25 strongest pixels within a radius of  $r_2$  pixels from the initial seed center in a gradient magnitude image calculated with convolutions with the kernels

$$\begin{bmatrix} -1 & 0 & 1 \\ -2 & 0 & 2 \\ -1 & 0 & 1 \end{bmatrix} \text{ and } \begin{bmatrix} -1 & -2 & -1 \\ 0 & 0 & 0 \\ 1 & 2 & 1 \end{bmatrix}$$

and equation 2 and  $T_{\text{Deriv}} \in [0, \infty)$  is a threshold value. The variable  $D$  is obtained by calculating the pixel intensity derivatives at the examined pixel in the directions towards all edge pixels in the previous ROI obtained with condition (a). The variable  $D$  is then

---

set to the maximum of the calculated derivatives.

4. A neighbouring pixel is first included if it satisfies the condition

- (a)  $I \geq M_1 \cdot T_1 + M_2 \cdot (1 - T_1)$  where  $I$  is the pixel intensity,  $M_1$  is the mean of the 7 strongest pixels in the local area,  $M_2$  is the mean of the 16 weakest pixels in the local area, and  $T_1 \in [0, 1]$  is a threshold value. The local area is defined as the region within a radius of  $r$  pixels from the initial seed center.

Once no neighbours satisfy this criterion, the following criterion is used

- (b)  $(D < 0) \wedge (I > S_{\min} + (S_{\max} - S_{\min}) \cdot T_2)$ . The variable  $I$  is the intensity in the examined pixel and  $T_2 \in [0, 1]$  is a threshold value. The other variables are derived by sampling points along a radial line starting at the center of the ROI obtained with equation (a) which goes through the examined pixel and continues outwards for a distance of 10 pixels. The variable  $D$  is the slope along this line at the examined pixel,  $S_{\min}$  is the mean of the 4 lowest sampled intensities along the line and  $S_{\max}$  is the highest sampled value along the line.

The first homogeneity criterion (criterion 1) was developed to behave in a way similar to pixel selection tools in image editing softwares where connected pixels of similar colors are selected.

Criterion 2(a) was an attempt to improve the previous method by exchanging the fixed pixel value threshold with a threshold based on the initial seed intensities. For example: include all pixels with an intensity greater than 70% of the mean seed intensity. Criterion 2(b) was intended to make the algorithm include pixels on the object edges where there is a strong gradient.

The goal of the third method was to first segment a flat region with an intensity threshold based on an intensity midway between the mean intensity of the object and the mean intensity of the background. Once the flat area had been segmented, the second criterion was intended to include pixels of the edge of the object identified by a high image gradient in the direction outwards from the object. The difference between criterion 2(b) and 3(b) is that criterion 2(b) uses the slope in the direction towards the starting pixel whereas criterion 3(b) uses slopes towards multiple pixels; the pixels obtained from criterion 3(a). Criterion 3(b) was developed to be less sensitive to the starting seed compared to criterion 2(b).

The fourth method re-used the intensity-based threshold from the third method to obtain an estimate of the center of the lymph node. The second part of the algorithm samples points along a line from the center of the lymph node outwards through the pixel examined to check if the pixel was part of the slope outwards or not. With a threshold of for example  $T_2 = \frac{1}{10}$ , the condition becomes: 'Include the pixel if it is part of an outward slope and if its intensity is within the full width at tenth maximum (FWTM)'. This technique is illustrated in figure 10.

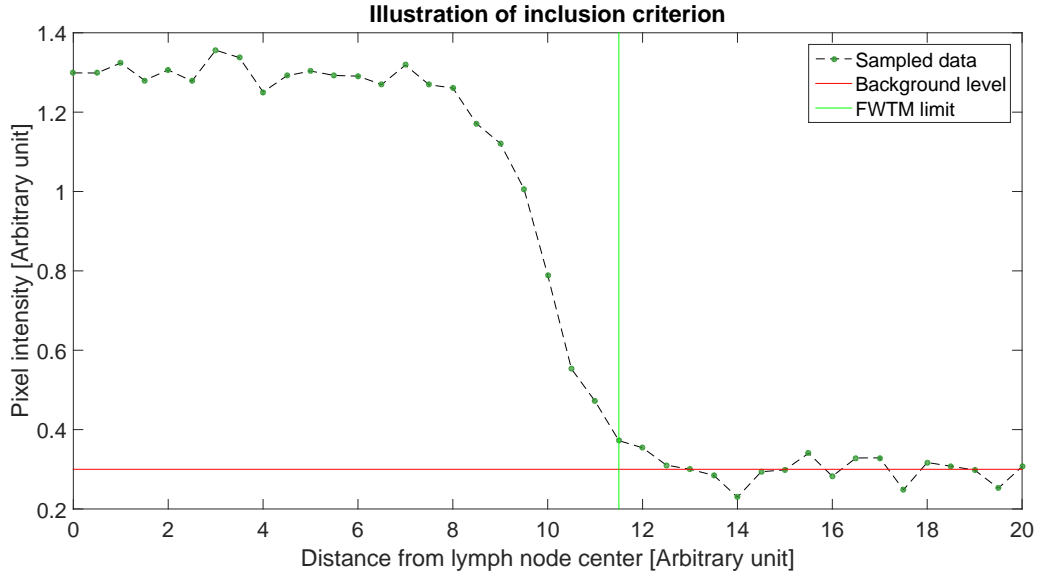


Figure 10: Illustration of inclusion criterion with synthetic data for demonstrative purposes. All sampled points to the left of the vertical line would have been accepted by the inclusion criterion with  $T_2 = \frac{1}{10}$ .

#### 4.2.2 Edge detection

For edge detection, two algorithms were tested; one from a MATLAB toolbox and one self developed algorithm. MATLAB's edge detection function, called `edge`, contained several edge detection methods. The default Sobel edge algorithm was used and the functions automatic threshold value selection was used. A drawback of MATLAB's function was that it only accepted 2D images. Thus, a custom algorithm was developed for evaluation of a possible 3D implementation.

The custom edge detection algorithm used the following nine-point-smoothing kernel

$$\begin{bmatrix} 1 & 2 & 1 \\ 2 & 4 & 2 \\ 1 & 2 & 1 \end{bmatrix} \cdot \frac{1}{16}$$

in a convolution with the image to reduce noise. The image gradients in the x- and y-directions were then obtained by convolving the image with the kernels

$$\begin{bmatrix} -1 & 0 & 1 \\ -2 & 0 & 2 \\ -1 & 0 & 1 \end{bmatrix} \text{ and } \begin{bmatrix} -1 & -2 & -1 \\ 0 & 0 & 0 \\ 1 & 2 & 1 \end{bmatrix}$$

respectively. These kernels are the Sobel approximations of the image gradients. The arrays with the resulting gradients were then used to obtain a gradient magnitude image using equation 2. The

---

edges in the image were then identified by thresholding the gradient magnitude image. The main differences between this algorithm and MATLABs function is that this algorithm lacks an automated threshold selection and an method for making the edges of the object one pixel thin. The advantage of this algorithm is that the extension to 3D segmentation by calculating the gradient in the third direction would be fairly simple.

### 4.2.3 Thresholding

Multiple thresholding methods were developed and evaluated. The following thresholding algorithms were used:

1. Global thresholding which included all pixels whose intensities  $I$  satisfied the criterion  $I \geq M_B \cdot T + M_O \cdot (1 - T)$ , where  $M_B$  is the lowest pixel intensity in the image,  $M_O$  the highest and  $T \in [0, 1]$  a threshold value.
2. Local thresholding which included all pixels whose intensities  $I$  satisfied the criterion  $I \geq M_B \cdot T + M_O \cdot (1 - T)$ , where  $M_B$  is the mean pixel value of the estimated background around an object marked with the crosshair,  $M_O$  is the mean pixel value of the estimated object marked with the crosshair and  $T \in [0, 1]$  a threshold value. The estimated object and background classifications were obtained by using a MATLAB function that calculates a threshold which minimizes the intraclass variance of the groups of pixels to be marked as object and background. The pixels used to calculate this threshold were limited to those within a radius of  $R$  pixels, specified by the user, from the crosshair center. Following the thresholding, only those pixels in the image which were connected to the object marked by the user were kept.
3. Local thresholding which included all pixels whose intensities  $I$  satisfied the criterion  $I \geq M_O \cdot T + M_B \cdot (1 - T)$ , where  $M_O$  is the mean of the 7 highest pixel intensities in the local area,  $M_B$  the mean of the 16 lowest pixel intensities in the local area and  $T \in [0, 1]$  a threshold value. The local area was specified as the area within a radius  $r$  around the crosshair, selected by the user. Following the thresholding, only those pixels in the image which were connected to the object marked by the user were kept.
4. Local automatic thresholding based on method 3. This method thresholded the image multiple times with the criterion  $I \geq k \cdot M/N$ , where  $I$  is the pixel intensity,  $k = 1, 2, 3, \dots, N$ ,  $M$  is the mean of the 7 highest pixel values in the local area and  $N$  the number of thresholdings. After each thresholding, the pixels in the image which were connected to the object marked by the user were counted. The algorithm then examined the number of counted pixels as a function of  $k$  for a large increase in the number of counted pixels. The lowest value of  $k$  where the increase in the number of pixels was greater than a threshold was selected as the threshold

---

value to be used in the criterion  $I \geq k \cdot M/N$ .

Method 4 was an attempt to solve the issue of segmented lymph nodes connecting to nearby structures. The idea was to lower the threshold gradually until the segmented area 'leaks' out into the nearby structures. When this happens, the number of pixels in the ROI was expected to have a sudden large jump as the two structures joined. This method is illustrated in figure 11.

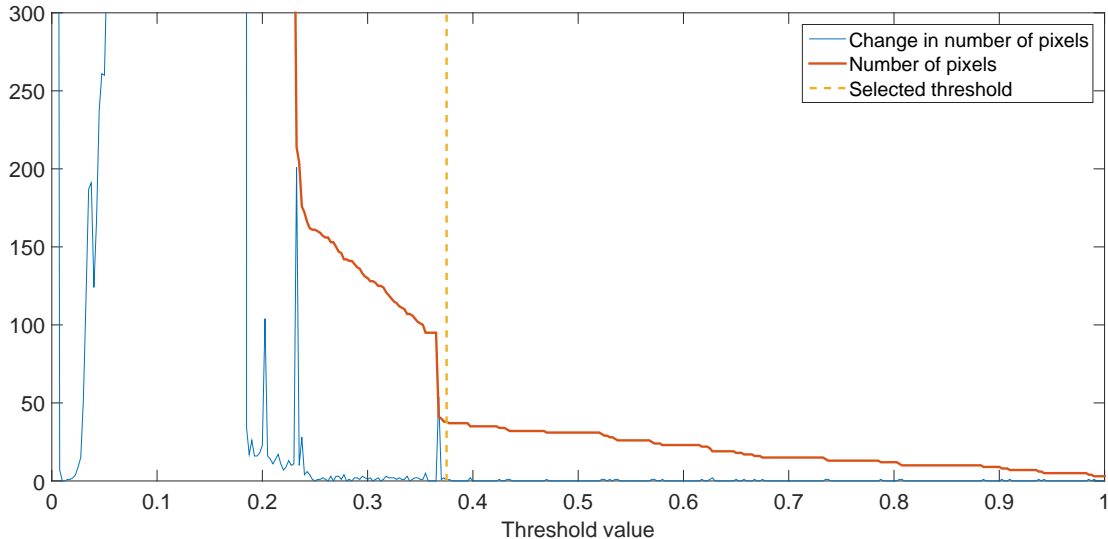


Figure 11: The number of pixels in the ROI and the change in number of pixels plotted as a function of the threshold value. A vertical line shows the selected threshold, which is located next to a large jump in the number of pixels.

#### 4.2.4 Fast marching method

A fast marching method for segmenting 2D images was available from a MATLAB toolbox. This function, called `imsegfmm`, required an initial seed, a pixel weight array and a threshold. Two accompanying functions were available for calculation of the weight array; one based on differences in pixel intensities, called `graydiffweight` and one based on gradient magnitude, called `gradientweight`.

Segmentations with both types of weight arrays were evaluated. For both methods, the user was allowed to specify the center of the initial seed, the seed radius and the threshold. For the method using differences in pixel intensities, a reference intensity was required for calculating the differences. The mean intensity of pixels in the specified seed was used for this reference intensity.



---

#### 4.2.5 2D ('spiral') scanning algorithm

A 2D scanning algorithm based on the algorithm used by Wang, J et al. [10] was developed and evaluated. The article by Wang, J et al. about the 3D spiral scanning technique only covered scanning in 3D data. The authors referred to earlier works in which 2D objects were converted to polar coordinates in their article. However, these articles did not explicitly describe the scanning process. The 2D scanning technique discussed in this chapter has been developed as a modification of the 3D scanning technique for scanning in a 2D image.

The 2D scanning algorithm started with a region growing algorithm with the homogeneity criterion  $I \geq M_1 \cdot T + M_2 \cdot (1 - T)$  to obtain an estimate of the object, where  $I$  is the intensity of the examined pixel,  $M_1$  is the mean of the 7 highest intensity in the local area,  $M_2$  is the mean of the 16 lowest intensities and  $T \in [0, 1]$  is a threshold value. The local area is defined as the region within a radius of  $r$  pixels from the initial seed center. The segmented pixels were then used to calculate a center  $(x_c, y_c)$  for the scanning algorithm. For the 2D spiral scanning algorithm, the azimuth angles  $\alpha_n$  were calculated as:

$$\begin{aligned} \alpha_n &= n \cdot \frac{2\pi}{N} \\ n &= 1, 2, 3, \dots, N \end{aligned} \quad (7)$$

where  $N$  is the number of scanning lines. For each azimuth angle  $\alpha_n$ , a direction  $\vec{V}_\alpha$  was calculated as:

$$\vec{V}_\alpha = (\cos(\alpha_n), \sin(\alpha_n)) \quad (8)$$

For each radial line  $\vec{V}_\alpha$  originating from the point  $(x_c, y_c)$ , samplings were made in the image  $f(x, y)$  at the coordinates

$$(x_c, y_c) + \vec{V}_\alpha \cdot R_m \quad (9)$$

where  $m = 1, 2, 3, \dots, 31$  and  $R_m = \frac{m-1}{2} = 0, 0.5, 1, \dots, 15$  defines the sampling distances, in pixels, from the origin. The maximum sampling distance of 15 pixels were chosen based on the sizes of the lymph nodes in the dataset and the voxel dimensions of the dataset. This sampling resulted in an image  $g(n, m)$ , where

$$g(n, m) = f(x_c + \cos(\alpha_n) \cdot R_m, y_c + \sin(\alpha_n) \cdot R_m) \quad (10)$$

A cubic interpolation method was used to acquire the image intensities where the radial lines didn't intersect the pixel centres. An example of sampling points with  $N = 100$  is shown in figure 12 and the resulting image  $g(n, m)$  is shown in figure 13.

Once a polar map was obtained, Wang, J et al. used a dynamic programming algorithm to find an optimal path through the image. Due to time restrictions and lack of knowledge about these types

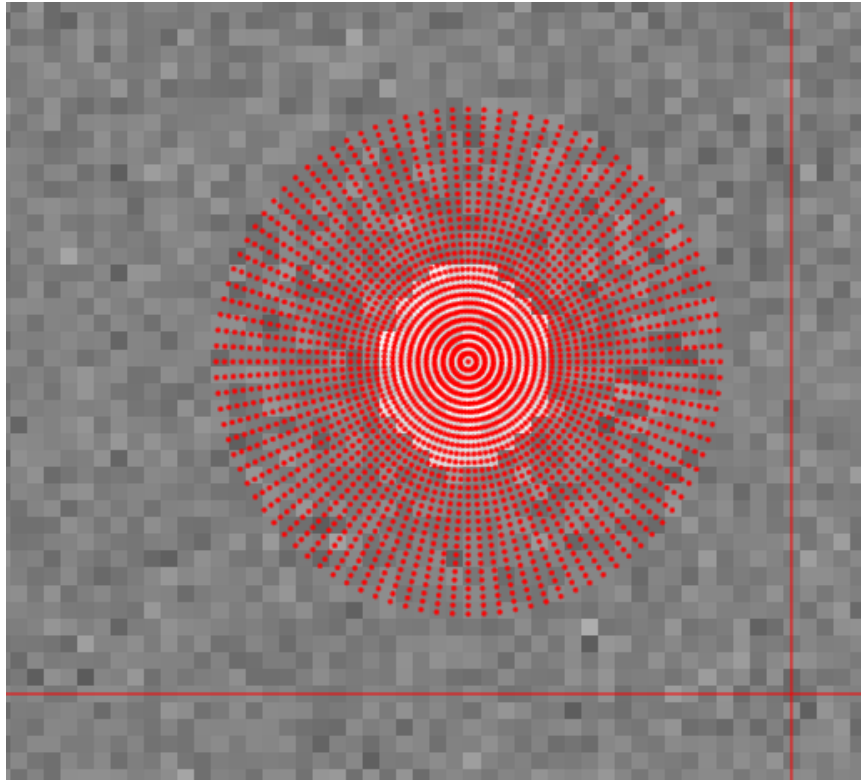


Figure 12: Sample points shown as dots in a simple artificial image.

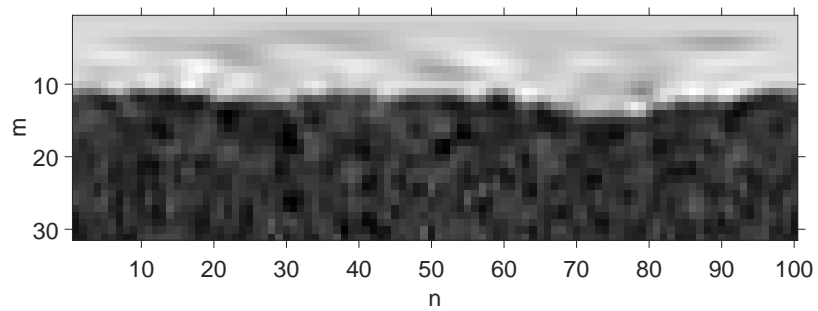


Figure 13: Resulting image after scanning. The upper rows corresponds to the lowest values of  $m$  and  $R_m$ . The leftmost columns corresponds to the lowest values of  $n$  and  $\alpha_n$ .

---

of algorithms, a simpler algorithm for finding a path was developed.

To find a path through the image, an iterative method was developed to find a path through  $g$  that followed the edge of the object. The idea of using an iterative method to find an edge was based on the active contours algorithm developed by Kass et al [14]. While regular active contours can move in both the x- and y-directions in an image, the contour in the image obtained from the scanning process only needed to move in the y-direction, which simplified the algorithm.

The y-coordinates of the path through the image was defined by a vector  $P$  with  $N$  elements where an element with index  $n$  corresponded to the paths y-coordinate in the image  $g$  in column  $n$ . The path through the image  $g$  was therefore given by the set of coordinates  $(n, P(n))$  where  $n = 1, 2, 3, \dots N$ . The iterative method used external forces derived from  $g$  to push the y-coordinates  $P(n)$  of the path towards the edge of the object. These external forces were used as a substitute for the external costs used by Wang et al. for finding the optimal path. The external forces were also a substitute for the external energies used by Kass et al. in the active contour model. To avoid large jumps in y-coordinates between nearby points on the path, the method also used internal forces which acted against such events. These internal forces were a substitute for the internal costs used by Wang et al. to keep the surface smooth as well as a substitute for the internal energy used by Kass et al. for controlling the curvature of the active contours.

The external forces were calculated before the iterative method was initiated. The forces in the y-direction, denoted  $F_E(n, m)$  were calculated for each point in the image  $g(n, m)$ . The external force on a point  $(n, P(n))$  on the path was then calculated as  $F_E(n, P(n))$ . Multiple ways of defining the external force  $F_E(n, m)$  were tested. Two methods worked successfully.

- Defining a potential energy  $U$  as

$$U(n, m) = w_1 \cdot \text{sgn} \left( \frac{\partial g(n, m)}{\partial m} \right) \cdot \left| \frac{\partial g(n, m)}{\partial m} / g_{\max}(n) \right|^2 + w_2 \cdot \frac{g(n, m)}{\max(g)} \quad (11)$$

where  $w_1$  and  $w_2$  are weight factors,  $\text{sgn}$  is the signum function defined as:

$$\text{sgn}(X) = \begin{cases} -1, & X < 0 \\ 0, & X = 0 \\ 1, & X > 0, \end{cases} \quad (12)$$

and  $g_{\max}(n)$  is a normalization function based on the maximum value of each column  $n$  in  $\frac{\partial g(n, m)}{\partial m}$ . The external force is then defined as

$$F_E(n, m) = -\frac{\partial U(n, m)}{\partial m}$$

---

The  $w_1$  gives a low potential energy if  $g(n, m)$  is decreasing as a function of  $m$  and the image gradient is large. This term is based on an edge functional used by the active contour in [14]. See expression/equation 6. The  $w_2$  term gives a low potential energy where  $g(n, m)$  has a low pixel intensity and is based on expression/equation 5. The external force is meant to push the path towards areas where the potential energy is low. The goal of this method is to have the path attracted to sharp slopes outwards with the  $w_1$  term. The  $w_2$  term is then meant to be used to adjust the size of the segmented object by attracting the edge outwards towards lower pixel intensities.

- Defining the external force as

$$F_E(n, m) = -w_1 \cdot \frac{\partial g(n, m)}{\partial m} \Big/ g_{\max}(n) - w_2 - w_3 \cdot \text{sgn} \left( \frac{\partial g(n, m)}{\partial m} \right) \cdot \frac{g(n, m)}{g(1, 1)} \quad (13)$$

The goal of this method is to have the initial path start outside the object and then push the path towards  $P(n) = 0$  with the  $w_2$  term. The  $w_1$  and  $w_3$  are meant to stop the path at strong edges in the image where  $\frac{\partial g(n, m)}{\partial m} < 0$ , i.e. at slopes outwards. The  $w_1$  term stops the path based on slope magnitude and  $w_3$  stops the path based on image intensities.

The internal forces were based on the y-coordinates  $P(n)$  of neighbouring points and were continuously calculated during the iterations. The internal force  $F_I$  on a point  $P(n)$  was calculated as

$$\begin{aligned} F_I(P(n)) = & k \cdot (P(n+1) + P(n-1) - 2 \cdot P(n)) + \\ & + \frac{1}{2} k \cdot (P(n+2) + P(n-2) - 2 \cdot P(n)) + \\ & + \frac{1}{4} k \cdot (P(n+3) + P(n-3) - 2 \cdot P(n)) \end{aligned} \quad (14)$$

where  $k$  is a spring constant. This expression was derived from the idea of adding spring forces between the point  $P(n)$  and its 6 closest neighbours. The force between  $P(n)$  and its neighbour  $P(n-1)$  was set to  $k \cdot (P(n-1) - P(n))$ . A similar force was applied between  $P(n)$  and  $P(n+1)$ . For the points  $P(n \pm 2)$ , a reduction factor of  $\frac{1}{2}$  was applied due to the points being further away and for  $P(n \pm 3)$  a factor of  $\frac{1}{4}$  was used. The internal forces are illustrated in figure 14.

An example of an external force acting on a point on the path is illustrated in figure 15.

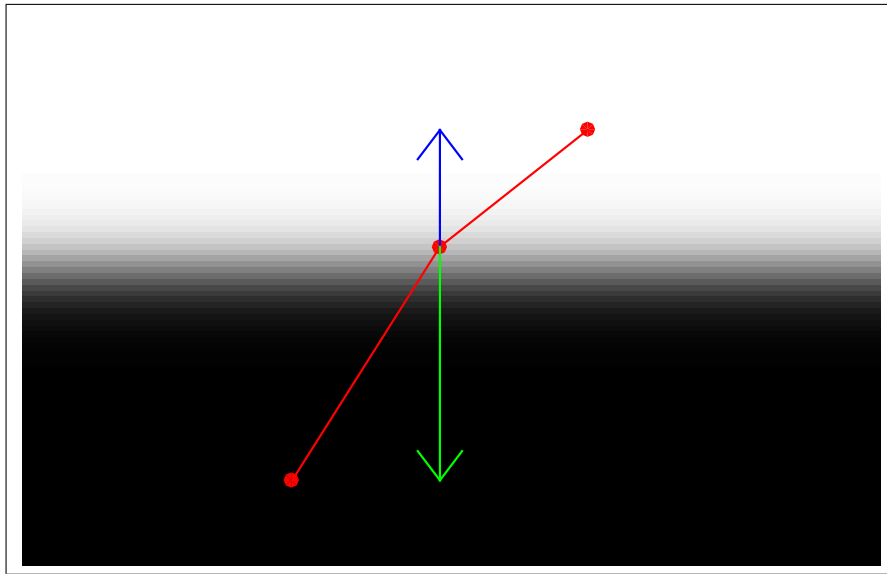


Figure 14: Illustration of internal spring forces on a single point from its nearest neighbours. The neighbour to the right exerts a spring force upwards on the middle point and the neighbour to the left exerts a greater spring force downwards. The forces exerted by the middle point on its neighbours, which would attract them towards the center of the image, are not shown.

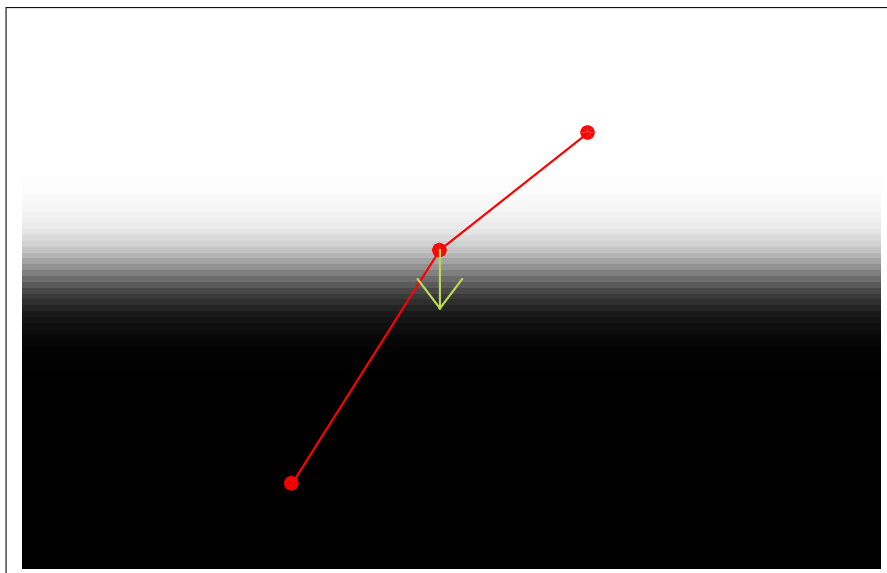


Figure 15: Illustration of external force acting on a single point. The external force shown in this figure attracts the point towards the greatest vertical image gradient in the image.

The iterative method used a method based on the Euler method for solving differential equations to move the path towards the edges in the image. In the Euler method, if a variable  $y$  satisfies the differential equation  $y' = f(t, y)$  and initial values  $y_0$  and  $t_0$  are given, then an approximate solution to the differential equation is given by the set of points  $(t_i, y_i)_{i=0}^m$ , where  $t_{i+1} = t_i + h$ ,  $y_{i+1} = y_i + h \cdot f(t_i, y_i)$ ,  $h$  is a step length,  $i = 0, 1, 2, \dots, m$  and  $m$  is the number of steps. With the positions of the path during the  $i$ 'th iteration denoted  $P(n)_i$ , then the positions during the next iteration was calculated as:

$$P(n)_{i+1} = P(n)_i + \Delta \cdot (F_E(n, P(n)_i) + F_I(P(n)_i)) \quad (15)$$

where  $\Delta$  was a step length multiplier for limiting the step lengths to reasonable lengths. The iterations continued until the largest change in value of the elements in  $P$  was below a threshold. The initial path positions  $P(n)_0$  were obtained with a method that roughly estimated where the lymph node edge was by checking for each pair of  $n$  and  $m$  if the criterion

$$\left( \frac{\partial g(n, m)}{\partial m} < T_{\text{Deriv}} \vee \frac{g(n, m)}{g(1, 1)} > T_1 \right) \wedge \neg \left( \frac{\partial g(n, m+1)}{\partial m} < T_{\text{Deriv}} \vee \frac{g(n, m+1)}{g(1, 1)} > T_1 \right)$$

was true. If the criterion was true for a given  $n$  and  $m$ , then  $P(n)_0$  was set to  $P(n)_0 = m$ . If multiple values of  $m$  satisfied the criterion for a fixed value of  $n$ , then  $P(n)_0$  was set to the lowest value of  $m$  for which the criterion was true. This method found the edge of a lymph node by stating that a pixel belongs to the lymph node if  $\left( \frac{\partial g(n, m)}{\partial m} < T_{\text{Deriv}} \vee \frac{g(n, m)}{g(1, 1)} > T_1 \right)$  is true and to the background if it is false. If this criterion was true for a point  $(n, m)$ , but false for a point  $(n, m+1)$ , then the point  $(n, m)$  was classified as a part of the lymph node edge. The edge pixels obtained this way were then used as the initial values for  $P(n)$ .

When the iterations had finished, the result was a set of coordinates  $(n, P(n))$  through the image  $g$ , where  $n = 1, 2, 3, \dots, N$  corresponds to the columns in  $g$ . For each of these columns, an azimuth angle  $\alpha_n$ , a radial line direction  $\vec{V}_\alpha$  were available. Since,  $P(n)$  corresponds to y-coordinates, or rows in  $g$  which in turn corresponds to values of  $m$  and sampling distances  $R_m$ , the path  $P$  through the image  $g$  could be transferred back into the image  $f$  via the radial lines used. For each path coordinate  $(n, P(n))$ , a point was placed in the image  $f$  at the coordinate  $\vec{H}_n$  given by:

$$\vec{H}_n = (x_c + \cos(\alpha_n) \cdot P(n), y_c + \sin(\alpha_n) \cdot P(n)) \quad (16)$$

An example of a path is shown in figure 16 and the result after projecting it back to the original image is shown in figure 17. No method for determining which pixels were inside and which pixels were outside the contour was developed.

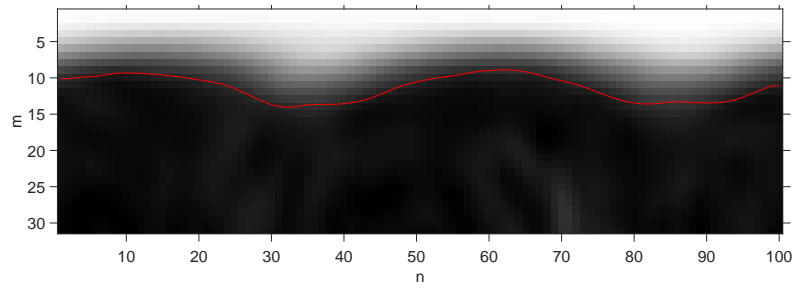


Figure 16: A path through the image  $g$  after the final iteration.

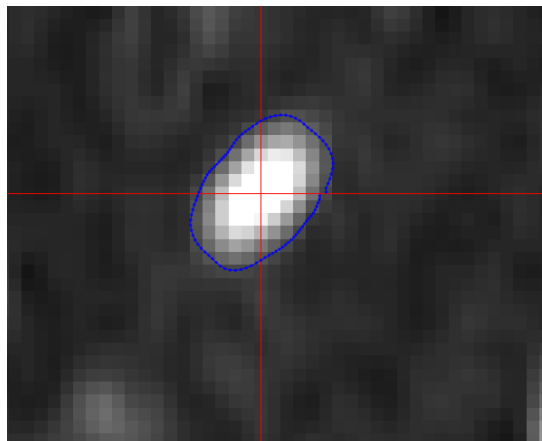


Figure 17: Resulting object edge in the image  $f$ .

---

#### 4.2.6 Active contour algorithm

An active contour algorithm, called `activecontour`, for segmenting 2D grayscale images was available from a MATLAB toolbox. Since it was limited to 2D images, it was primarily used for comparison with other algorithms performances. The algorithms standard settings were used.

### 4.3 Development of primary program

A primary program was developed for use by radiologists to view and segment selected lymph nodes in multislice DWI images. The program was given the following functions:

- Reading data from sets of diffusion weighted images and identifying the sets acquired with the highest b-value
- Reading the ADC data corresponding to the DWI data
- Displaying transverse, sagittal and coronal slices from the DWI and ADC data
- Segmenting lymph nodes selected by the user in 3 dimensions
- Overlaying the resulting VOIs on the displayed data
- Extracting and presenting information on lymph nodes using the VOIs and ADC data
- Saving the data to Excel files
- Display a histogram of the ADC values of the lymph nodes

A screenshot of the program is shown in figure 18.

#### 4.3.1 Segmentation algorithm

The segmentation technique selected to be used in this program was a 3D spiral scanning algorithm. This type of segmentation technique was chosen because of the performance of the 2D scanning algorithm in the segmentation evaluation program. Both the 2D scanning algorithms and the region growing algorithms utilizing image gradients were able to segment most lymph nodes and were considered for use in the primary program. The 2D scanning algorithms were selected for integration into the primary program because the segmentation of the object in the 2D k-r-space wouldn't require any major modifications; the segmentation would be in a 2D image in the k-r-space both in the 2D scanning technique and in a 3D scanning technique.

The 3D scanning algorithm used radial line directions defined with equation 3 and 4 with  $k = 1, 3, 5, \dots, 2N^2$  and  $N = 100$ . The variable  $N$  was set to 100 based on results during the initial development of the 2D scanning algorithms. When less than 100 lines per revolution was used, then



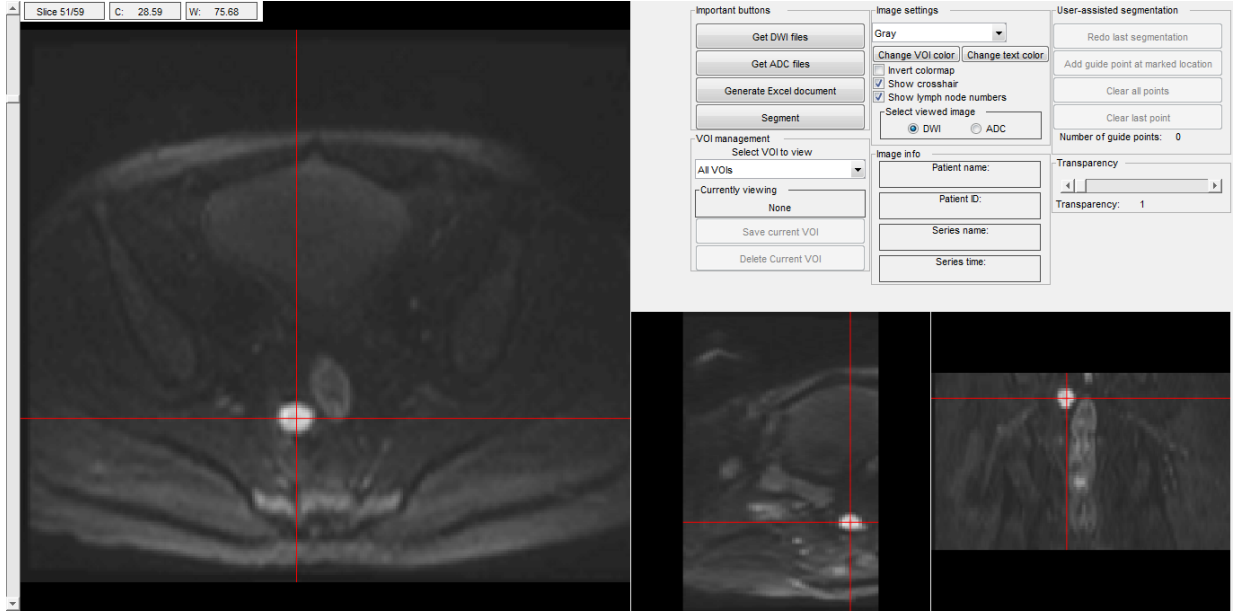


Figure 18: Screenshot of the primary program.

the 2D scanning algorithms would sometimes fail to delineate the contours of elongated objects. This number of lines per revolution was kept in the 3D scanning algorithm. The effect of changing the number of lines per revolution was not investigated in the 3D scanning algorithm. The reason for using only uneven numbers for  $k$  was that the resulting azimuth and elevation angles  $\alpha$  and  $\beta$  would be able to form a skewed  $N \times N$  grid for interpolations and surface plots when  $k$  produced  $N^2$  sampling directions. This feature was later scrapped but the definition of  $k$  remains. For the 3D scanning algorithm, the variable  $n$  denotes the  $n$ :th scanning direction. I.e.  $n = \frac{k+1}{2} = 1, 2, 3, \dots, N^2$ . For this algorithm, the azimuth and elevation angles will be denoted:

$$\begin{aligned}
 n &= 1, 2, 3, \dots, N^2 \\
 \alpha_n &= \frac{(2n-1) \cdot \pi}{N} \\
 \beta_n &= \frac{(2n-1) \cdot \pi}{2 \cdot N^2} - \frac{\pi}{2}
 \end{aligned} \tag{17}$$

In this algorithm, samplings along the radial lines were made at the distances  $R_m = \frac{m-1}{2} \cdot V_{\min}$  from the center of the sampling, where  $m = 1, 2, 3, \dots, 41$  and  $V_{\min}$  is the shortest voxel side length, in mm. The reason for this choice of sampling was to minimize distortions due to different voxel lengths in the  $X$ ,  $Y$  and  $Z$  directions. If a voxel had the dimensions  $2 \times 2 \times 5$  mm where 5 mm was the slice thickness, then a spherical lymph node was expected to be distorted in the image  $g$  if the samplings had used voxel indices as coordinates in the multislice data instead of coordinates in millimetres in the data.

---

Both types of external forces  $F_E(n, m)$  used in the 2D spiral scanning algorithm were initially tested, but the first type was later removed as the second yielded better results in terms of correctly finding and delineating entire lymph node surfaces. The internal force  $F_I(P(n))$  from the 2D algorithm was modified to include additional terms which attracted points with the same longitudes. In equation 17,  $\alpha_n$  has the property of

$$\alpha_{n+N} = \frac{(2(n+N)-1) \cdot \pi}{N} = \frac{(2n-1) \cdot \pi}{N} + \frac{2\pi N}{N} = \alpha_n + 2\pi$$

i.e. the path  $P$  always has  $N$  points per turn. The two points on the path  $P$  through the sampled image  $g$  with azimuth angles  $\alpha_n$  and  $\alpha_{n+N}$  will have the same longitude, since the coordinates  $X$  and  $Y$  in equation 4 are unaffected by adding  $2\pi$  to the azimuth angle  $\alpha$ , and can thus be considered neighbours in the latitude direction. This property of the coordinates  $X$  and  $Y$  also implies that the azimuth angle  $\alpha = \text{mod}(\alpha_n, 2\pi)$  and  $\alpha_n$  indicates the same longitude.

With spring forces between neighbouring points in the latitude direction added to the internal force  $F_I(P(n))$ , the result is:

$$\begin{aligned} F_I(P(n)) = & k \cdot (P(n+1) + P(n-1) - 2 \cdot P(n)) + \\ & + \frac{1}{2} k \cdot (P(n+2) + P(n-2) - 2 \cdot P(n)) + \\ & + \frac{1}{4} k \cdot (P(n+3) + P(n-3) - 2 \cdot P(n)) + \\ & + k \cdot (P(n+N) + P(n-N) - 2 \cdot P(n)) + \\ & + \frac{1}{2} k \cdot (P(n+2N) + P(n-2N) - 2 \cdot P(n)) + \\ & + \frac{1}{4} k \cdot (P(n+3N) + P(n-3N) - 2 \cdot P(n)) \end{aligned} \quad (18)$$

These spring forces between nearby points is a simplification, since it only considers neighbours in a cross-shaped pattern in the longitude and lateral directions. An alternative would be to consider all neighbours within a box or a circle in the longitude-latitude grid.

This internal force together with an external force was then used in an iterative process using equation 15 to move the path towards the object edge. When the iteration had converged, the set of path points  $(n, P(n))$  needed to be transformed into a VOI in the multislice data. For each path coordinate  $(n, P(n))$ , there is an associated azimuth and elevation angle  $\alpha_n$  and  $\beta_n$ . One way to visualize this data is to plot  $P(n)$  against  $\text{mod}(\alpha_n, 2\pi)$  and  $\beta_n$ . This visualization is shown in figure 19.

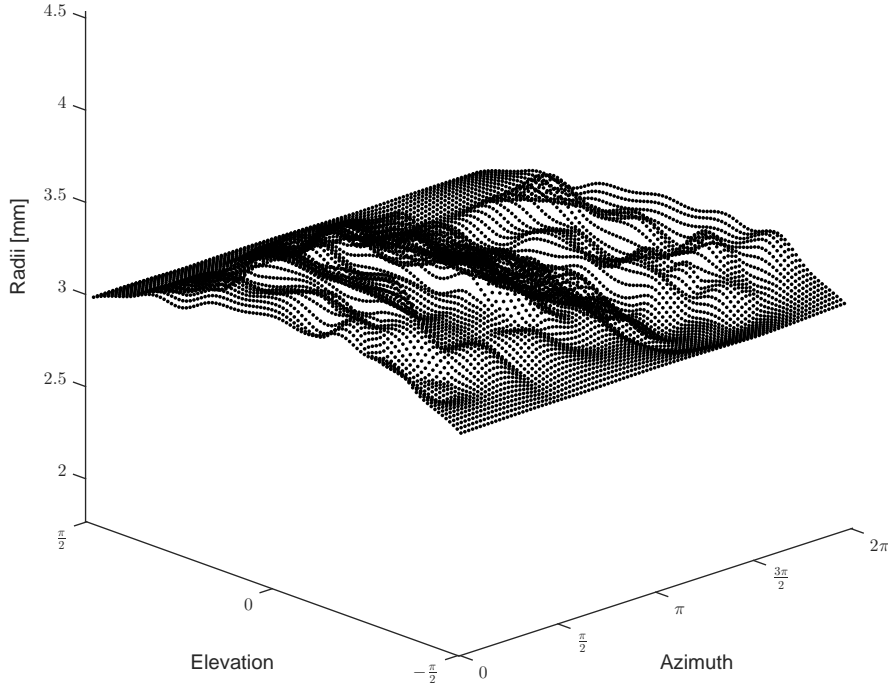


Figure 19: Surface plot of  $P(n)$  (Radii) plotted against  $\text{mod}(\alpha_n, 2\pi)$  and  $\beta_n$ .

Since  $P(n)$  represents a distance from the scanning center and  $\alpha_n$  and  $\beta_n$  indicates a direction, the surface of the object can also be visualized as the set of points  $V_n$ , where:

$$\begin{aligned}
 V_n &= (X, Y, Z) \\
 X &= P(n) \cdot \cos(\beta_n) \cdot \cos(\alpha_n) \\
 Y &= P(n) \cdot \cos(\beta_n) \cdot \sin(\alpha_n) \\
 Z &= P(n) \cdot \sin(\beta_n)
 \end{aligned} \tag{19}$$

An example of this visualization is shown in figure 20.

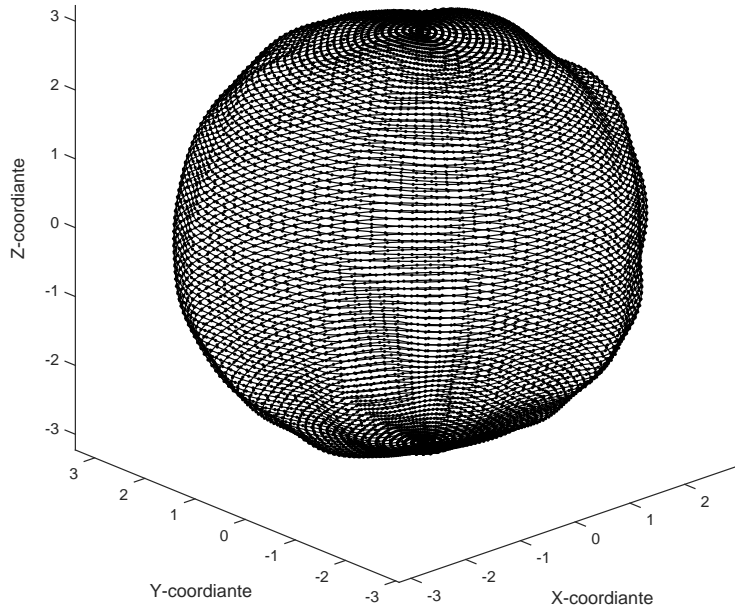


Figure 20: Visualization of a surface corresponding to the object shown in figure 4.

To obtain a VOI in the multislice data from the points  $(n, P(n))$ , the voxels in the multislice data that were located inside the surface in figure 20 had to be determined. To determine this, the Cartesian coordinates  $(X, Y, Z)$  of the voxels in the multislice data were converted to the spherical coordinates  $(\alpha, \beta, R)$  with the scanning center as the origin. A voxel with  $R(\alpha, \beta)$  was then compared to the surface shown in figure 19 given by the function  $S$

$$S(\text{mod}(\alpha_n, 2\pi), \beta_n) = P(n)$$

Since the values of the function  $S$  were only known at the points given by  $\text{mod}(\alpha_n, 2\pi)$  and  $\beta_n$ , interpolations were made using a linear interpolation method to obtain  $S(\alpha, \beta)$ . A voxel was then assumed to lie below the surface shown in figure 19 if  $R(\alpha, \beta) \leq S(\alpha, \beta)$ .

#### 4.3.2 Initial evaluation of the segmentation algorithm

The segmentation algorithm was evaluated with varying values for the segmentation parameters  $w_1, w_2, w_3$  and  $k$  on lymph nodes in DWI images to identify a set of parameters that performed the best in terms of the ability to segment lymph nodes with varying sizes, shapes, signal strengths and background structures well.

The segmentation technique and its general capabilities and behaviours on other objects was also assessed qualitatively by selecting elongated structures such as nerves and noting the results of the segmentations.

---

#### 4.4 Evaluation of primary program by radiologists

The primary program was tested by two radiologists in four patients with primary rectal cancer judged as advanced disease requiring neo-adjuvant chemoradiotherapy with 50–50.4 Gy given as 25–28 fractions in combination with capecitabine (Xeloda®). The evaluation was done on images acquired before and after chemoradiotherapy for each patient with a time period of about 3 months between the image acquisitions. Peri-rectal lymph nodes inside the perirectal fascia and nodes along the mesenteric vessels were manually targeted and evaluated by the program. Nodes not judged to be involved in the rectal cancer, e.g. nodes in the groin, were not evaluated. Lymph node volumes, mean ADC values per lymph node were acquired using the program. The total volume of all lymph nodes before and after the treatment was compared. The change in ADC and volume per lymph node was also. Additionally, the histogram function of the program was used to evaluate a large lymph node before, during and after chemoradiotherapy in one patient.

---

## 5 Results

### 5.1 Evaluation of segmentation techniques

#### 5.1.1 Region Growing

The first region growing method did not work sufficiently well neither in terms of separating lymph nodes from background structures nor in terms of segmenting different lymph nodes without changing the threshold value. These issues are illustrated in figures 21–23. The seed point is indicated by the red crosshair.

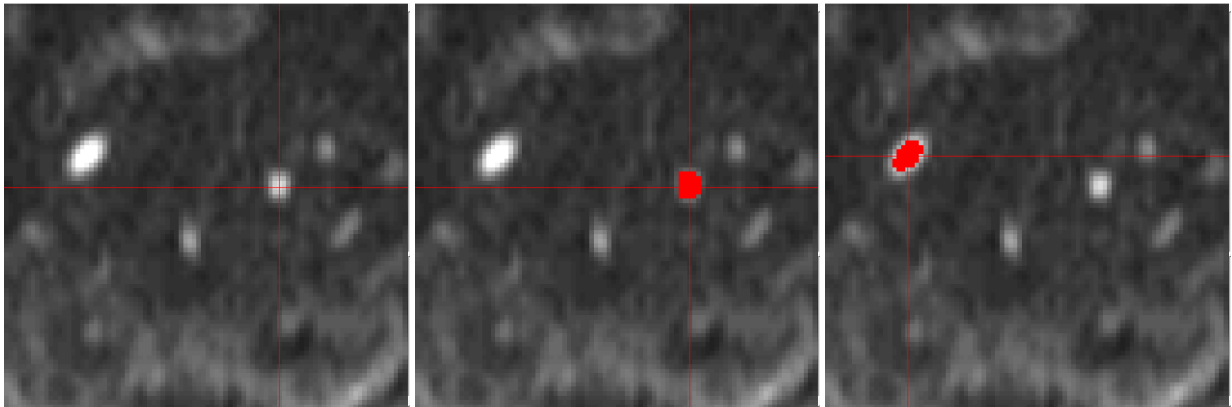


Figure 21: Pelvic lymph nodes before segmentation.

Figure 22: Segmentation of one lymph node.

Figure 23: Insufficient segmentation of another lymph node with the same threshold.

The second method was better at segmenting multiple lymph nodes with the same parameters, but didn't fully segment some lymph nodes with non-circular shapes and lymph nodes with nearby structures. This method is illustrated in figures 24–26.

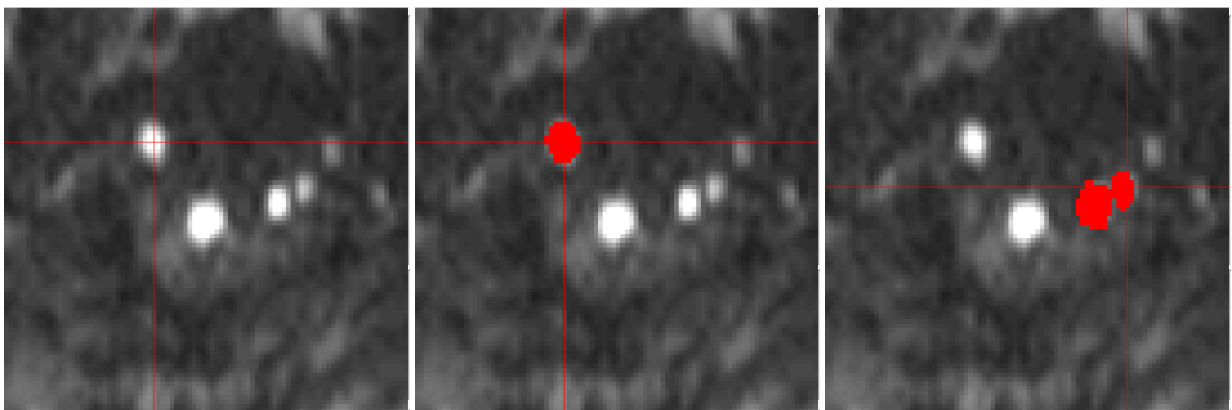


Figure 24: Pelvic lymph nodes before segmentation.

Figure 25: Segmentation of one lymph node.

Figure 26: Failed segmentation of another lymph node.

The third method could segment single lymph nodes well, but it could not segment multiple lymph nodes with the same set of parameters.

---

The fourth method was able to segment most lymph nodes well with the same parameters, but sometimes had issues with nearby structures. Results of this algorithm is shown in figures 27–31.

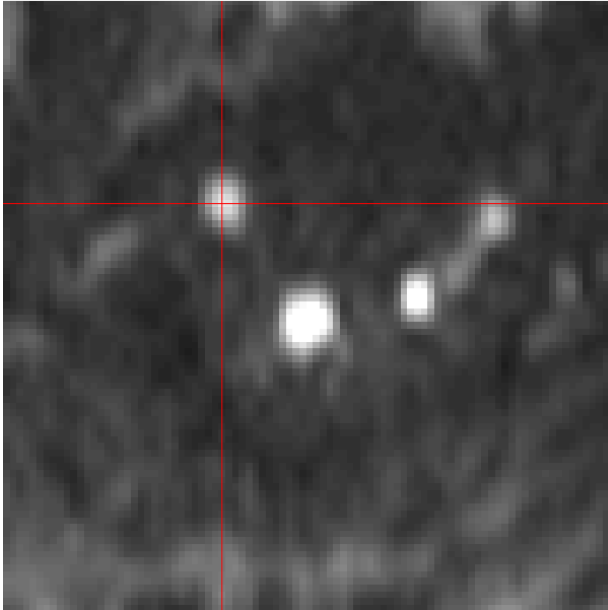


Figure 27: Pelvic lymph nodes before segmentation.

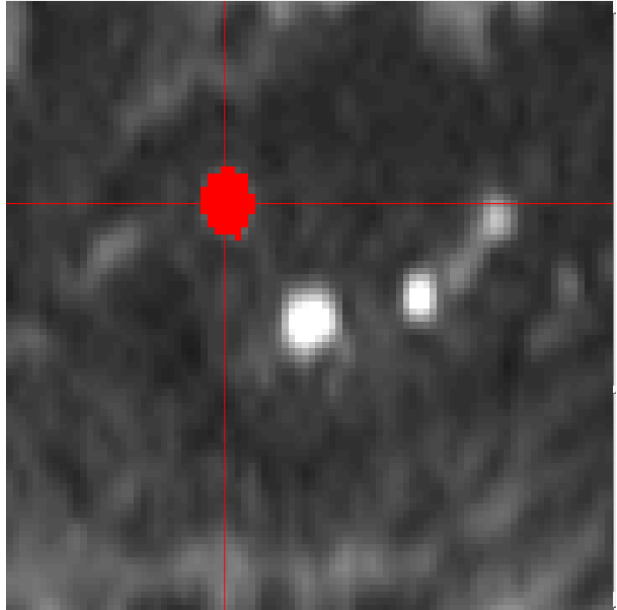


Figure 28: Segmentation of lymph node.

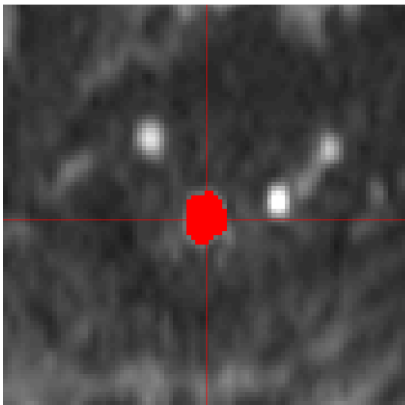


Figure 29: Segmentation of lymph node.

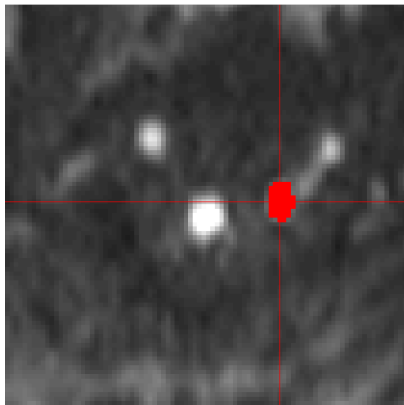


Figure 30: Segmentation of lymph node.

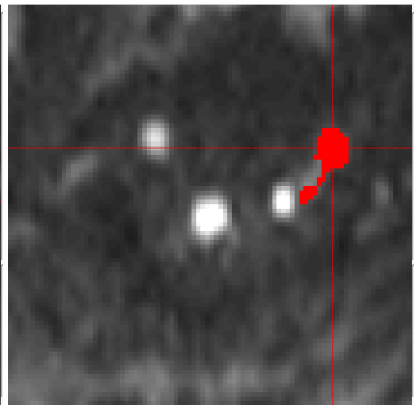


Figure 31: Failed segmentation of lymph node.

### 5.1.2 Edge Detection

The algorithm from MATLAB had mixed results. Some lymph nodes were surrounded fully by identified edges but most had gaps in their borders. The resulting objects enclosed by the edges were also generally smaller than expected.

The custom algorithm had also difficulties. The optimal threshold varied between different lymph nodes. A threshold that would segment one lymph node well would not work for another lymph node. Lymph nodes with adjacent structures were also hard to segment as the boundary between

the lymph node and the adjacent object would require one threshold whereas the rest of the lymph node edges had another optimal threshold. Therefore, this approach was considered to be difficult to develop for segmentation in 3 dimensions. The algorithms are shown in figures 32–34.

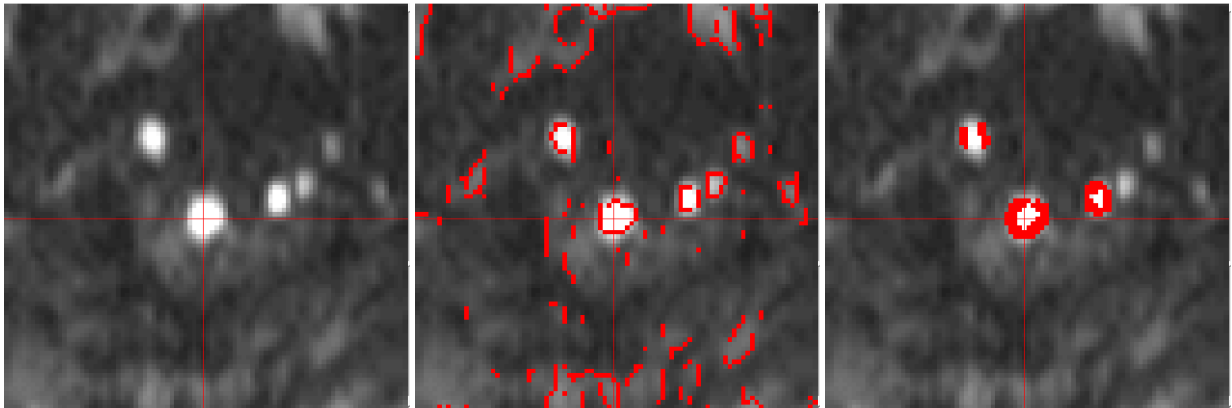


Figure 32: Pelvic lymph nodes before segmentation.

Figure 33: Results from the MATLAB Sobel operator.

Figure 34: Results of the custom algorithm.

### 5.1.3 Thresholding

Method 1 worked well in simple situations with lymph nodes surrounded by a background with low pixel intensity. The method was able to segment several such lymph nodes without changing the threshold. However, the method did not work equally well when there were objects or structures close to the lymph node. In these situations the segmented pixels of the lymph node and the nearby structure would become connected. When the threshold  $T$  was lowered, the objects would be separated, but the lower threshold would yield generally worse results.

Method 2 and 3 worked better than method 1 in terms of segmenting lymph nodes without needing to change the thresholds, but both still failed to segment some lymph nodes with nearby structures. Method 2 is illustrated in figures 35–38.

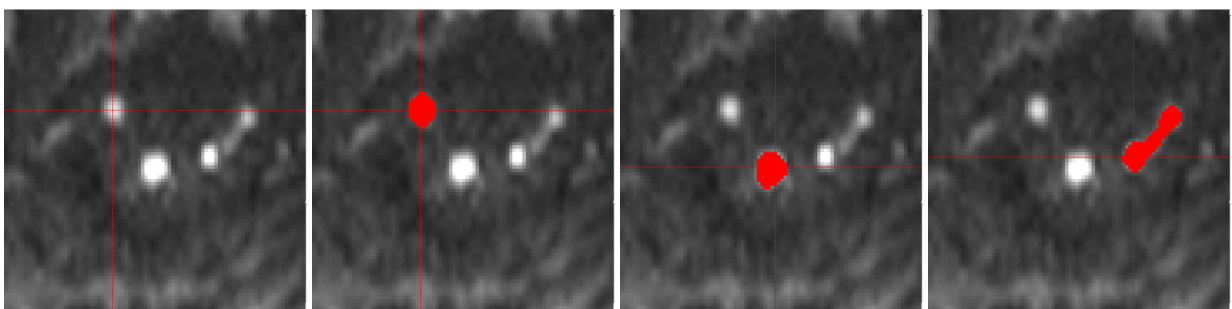


Figure 35: Pelvic lymph nodes before segmentation.

Figure 36: Segmentation of lymph node.

Figure 37: Segmentation of lymph node.

Figure 38: Failed segmentation of lymph node.



---

Method 4 worked successfully for a few lymph nodes with nearby structures, but still failed sometimes. For most lymph nodes, the previous methods worked better. This method is shown in figures 11 and 39.

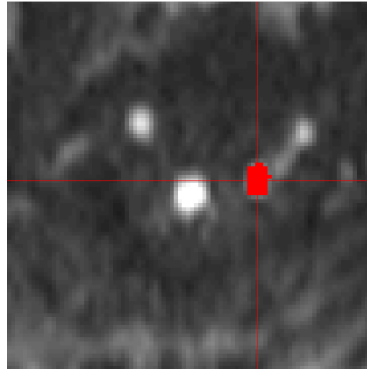


Figure 39: Segmentation of lymph node with method 4. The data related to the selection of the threshold which yielded this result is shown in figure 11.

The conclusion of the thresholding techniques was that they were unsuitable for lymph nodes with nearby objects and structures and that a well-working algorithm for segmentation in 3 dimensions would be difficult to develop.

---

#### 5.1.4 Fast marching method

The method based on differences in pixel intensities was capable of segmenting lymph nodes. However, the threshold had to be carefully chosen for each lymph node and the technique often leaked into the background. The method based on gradient magnitude had similar difficulties and is illustrated in figures 40 and 41.

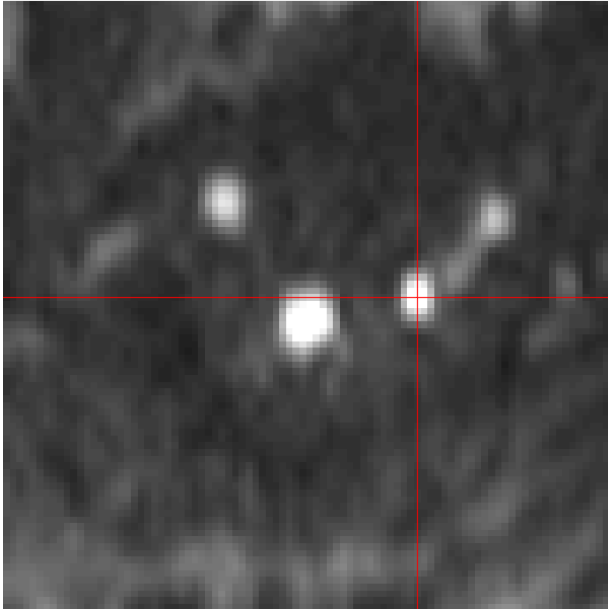


Figure 40: Pelvic lymph nodes before segmentation.

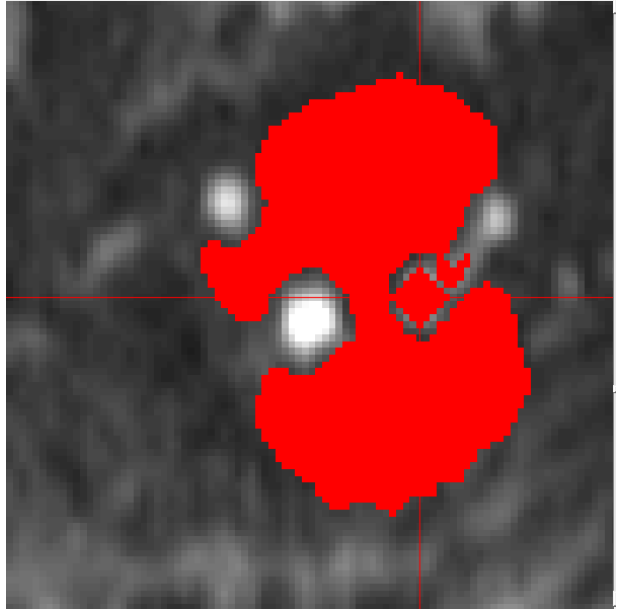


Figure 41: Failed segmentation of lymph node.

#### 5.1.5 2D scanning algorithm

After some test with different values for the weight factors  $w$  and the spring constant  $k$ , both algorithms were able to separate lymph nodes from background structures. The algorithms also worked well in terms of segmenting multiple lymph nodes using the same algorithm parameters. The conclusion about these algorithms were that both were valid candidates for further development for 3D segmentation. Results from the algorithm using the second external force is shown in figures 42–52.

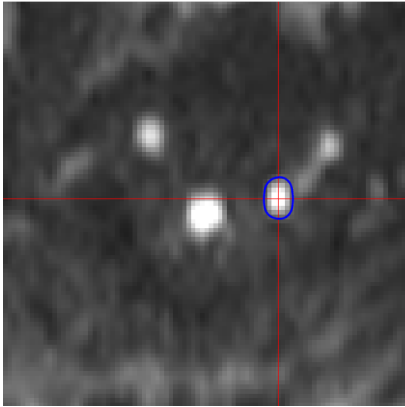


Figure 42: Segmentation of lymph node.

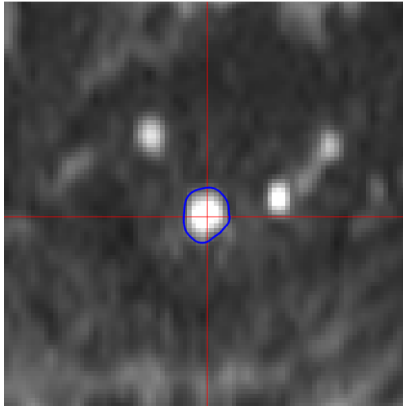


Figure 43: Segmentation of lymph node.

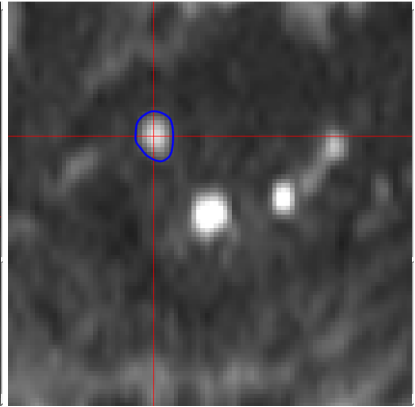


Figure 44: Segmentation of lymph node.

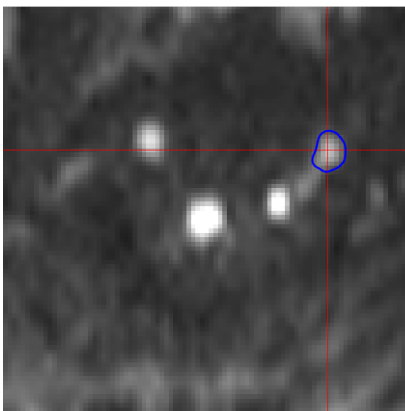


Figure 45: Segmentation of lymph node.

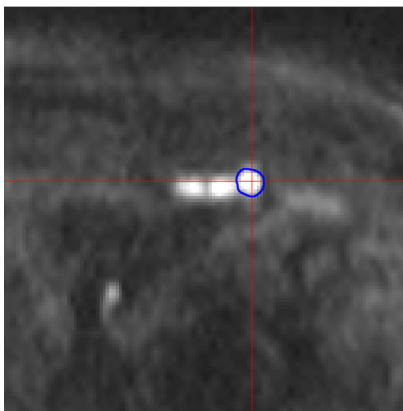


Figure 46: Segmentation of lymph node.

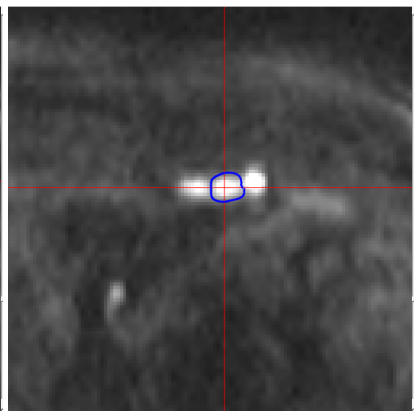


Figure 47: Segmentation of lymph node.

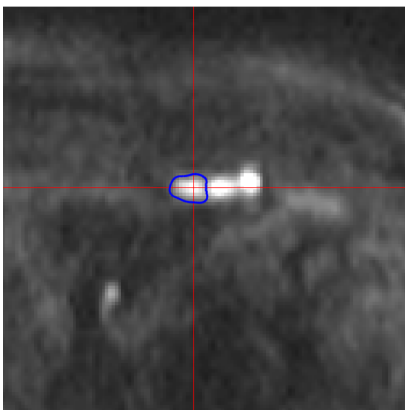


Figure 48: Segmentation of lymph node.

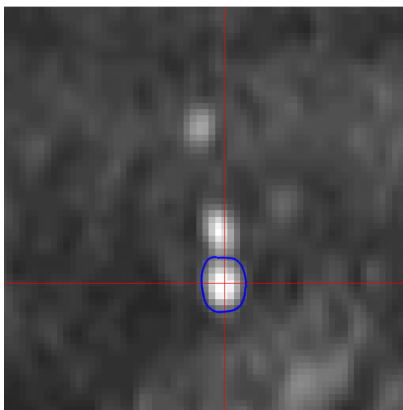


Figure 49: Segmentation of lymph node.

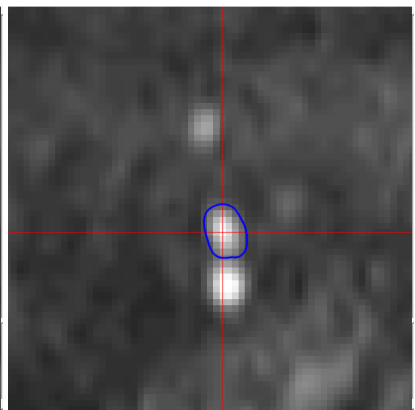


Figure 50: Segmentation of lymph node.

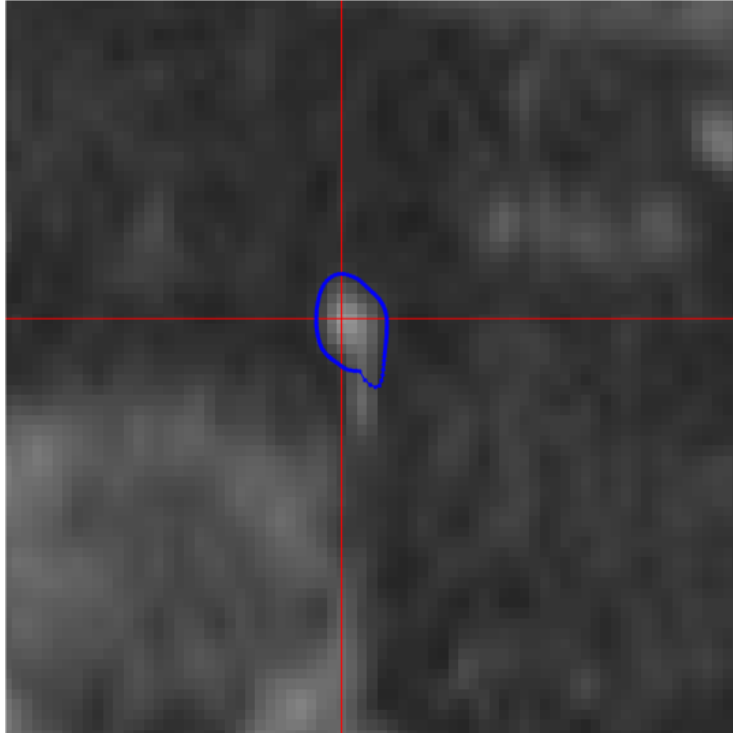


Figure 51: Failed segmentation of elongated object. Part of the bottom of the object is outside the contour.

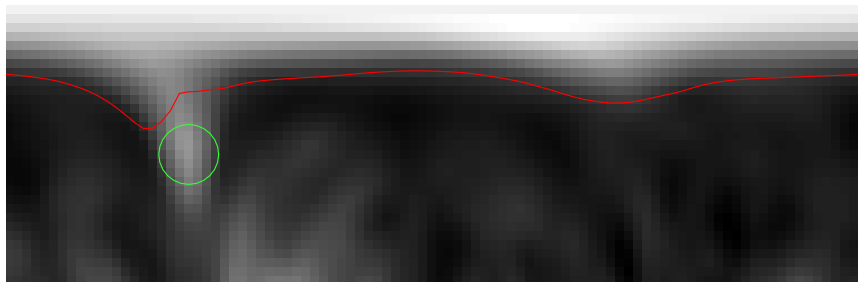


Figure 52: The path through the image  $g$  associated with the contour in figure 51. The part of the object in figure 51 that is outside the contour is associated with the outgrowth marked by a circle.

---

Results from the algorithm using the first external force is shown in figures 53–58. In figure 56, part of the contour has been initiated too far away from the lymph node edge to be attracted to it. The contour is discontinuous because there isn't a spring force between the first and last point on the path. A similar problem where the path doesn't fully follow the contour of a lymph node is shown in figure 57 and the corresponding image in the k-r-space is shown in figure 58.

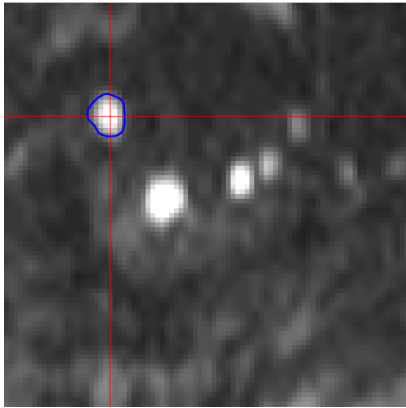


Figure 53: Segmentation of lymph node.

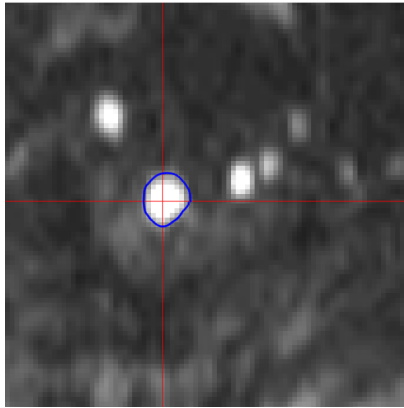


Figure 54: Segmentation of lymph node.

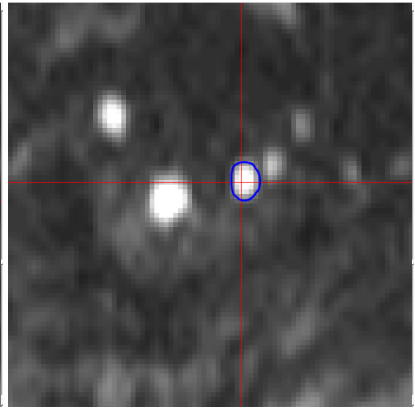


Figure 55: Segmentation of lymph node.

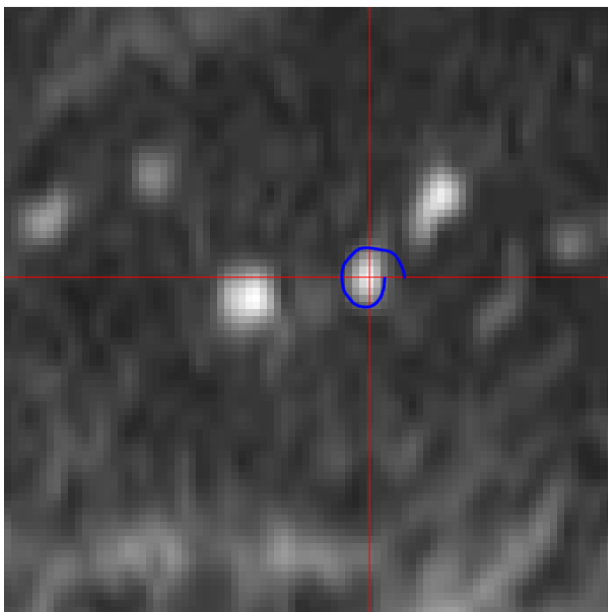


Figure 56: Segmentation of lymph node.

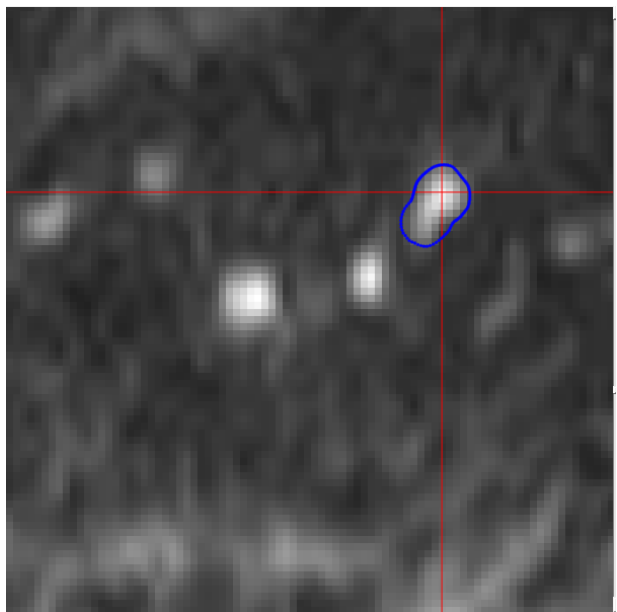


Figure 57: Segmentation of lymph node.

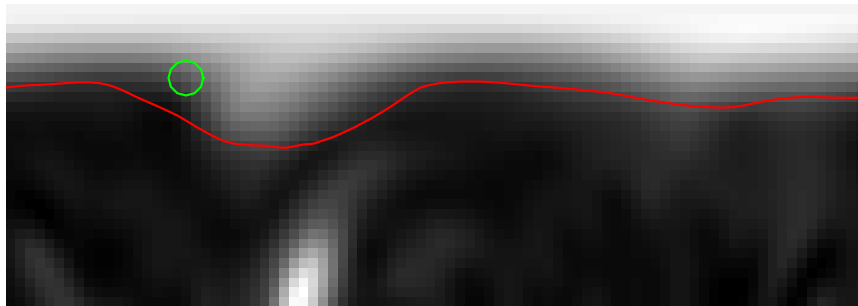


Figure 58: The path through the image  $g$  associated with the contour in figure 57. A part of the path that fails to follow the lymph node contour is marked by a circle.

### 5.1.6 Active contour algorithm

The active contour algorithm is demonstrated in figures 59–62. The algorithm was capable of separating lymph nodes from nearby structures and worked well in most lymph nodes. However, it would sometimes fail as seen in figure 62.

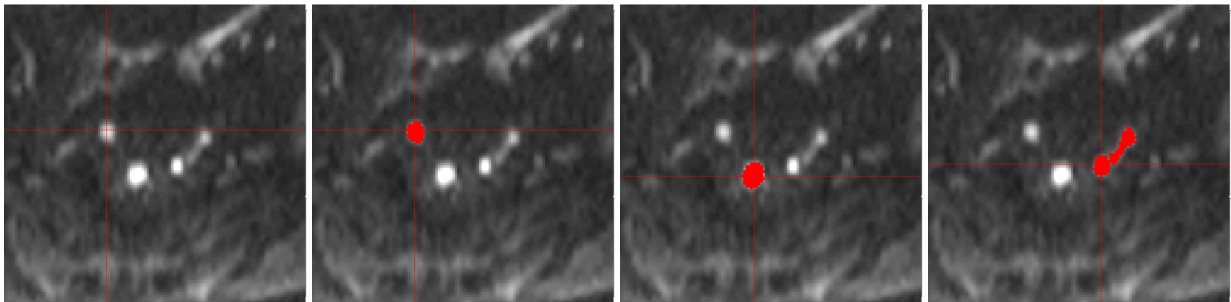


Figure 59: Pelvic lymph nodes before segmentation.

Figure 60: Segmentation of lymph node.

Figure 61: Segmentation of lymph node.

Figure 62: Failed segmentation of lymph node.

---

## 5.2 3D spiral scanning segmentation results

Figure 63 shows several slices of a lymph node that has been segmented using the 3D spiral scanning algorithm.

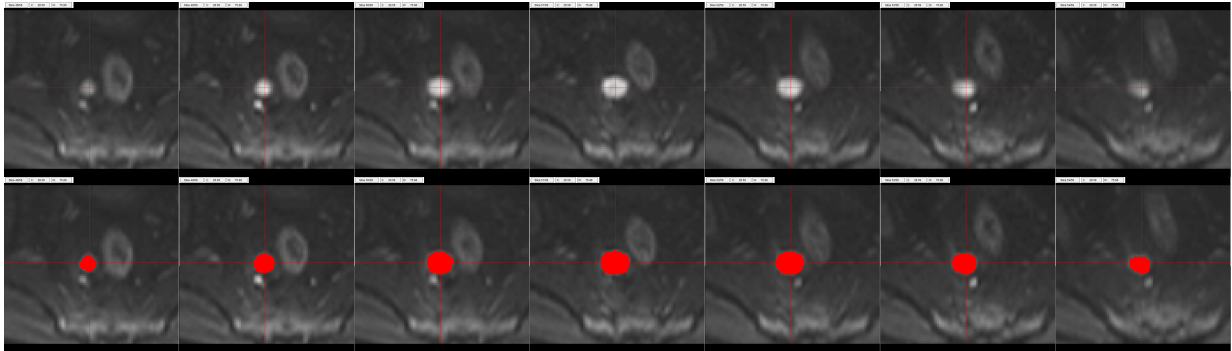


Figure 63: Transverse slices of a large lymph node is shown in the upper row and the result after the segmentation is shown in the lower row.

The lymph node surface is shown in figure 64.

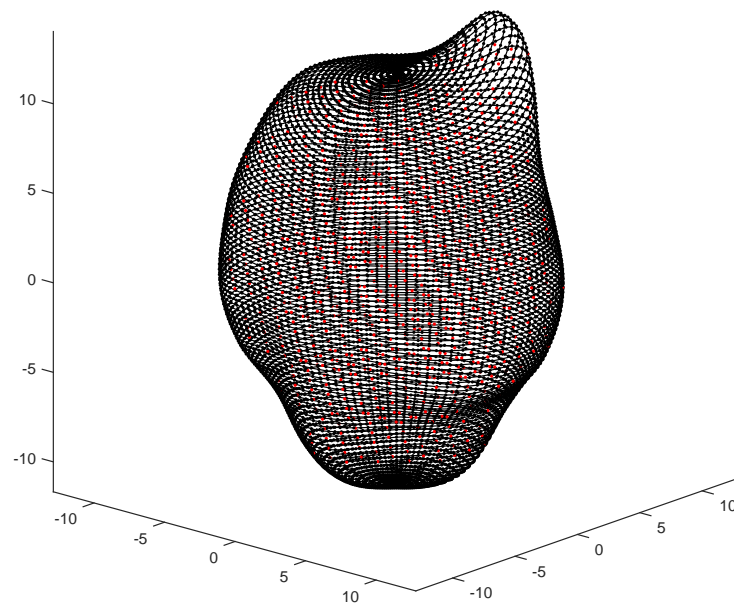


Figure 64: Visualization of the surface of the lymph node shown in figure 63.

Figure 65 shows the segmentation of another lymph node with an adjacent structure in the last slices.

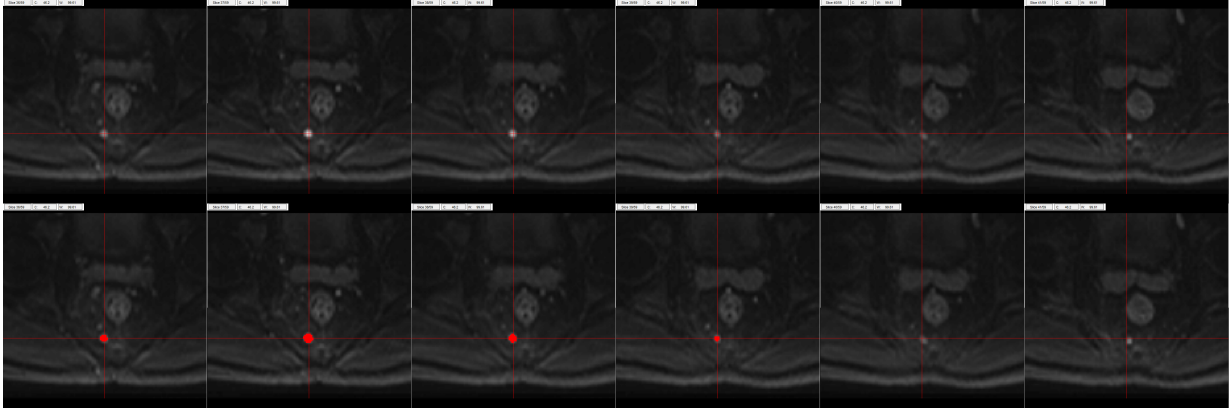


Figure 65: Transverse slices of a lymph node is shown in the upper row and the result after the segmentation is shown in the lower row.

An example of data extracted from the ADC images using the VOIs from the segmentations is shown in table 2.

Table 2: Data on the two lymph nodes shown in figures 63 and 65.

Lymph node	Slice	Number of voxels	Volume [ $\mu\text{L}$ ]	Mean ADC	Std. ADC
Lymph node 1	48-55	909	3740	889	197
Lymph node 2	36-39	112	461	982	219

The ADC values have the unit  $10^{-6} \text{ mm}^2 \text{ s}^{-1}$ .

The average time required to segment an object was 12 s on an ASUS laptop with a 2.13 GHz Intel Core i3-330M CPU when the execution time was evaluated on 13 objects with different sizes and shapes.



### 5.3 Evaluation of primary program by radiologists

The program was tested by two radiologists to obtain lymph node volumes and ADC values in four patients before and after chemoradiotherapy. Obtained data is shown in figures 66 and 67. Lymph nodes that are present before treatment but not after were not visible on the images or were unsuccessfully segmented.

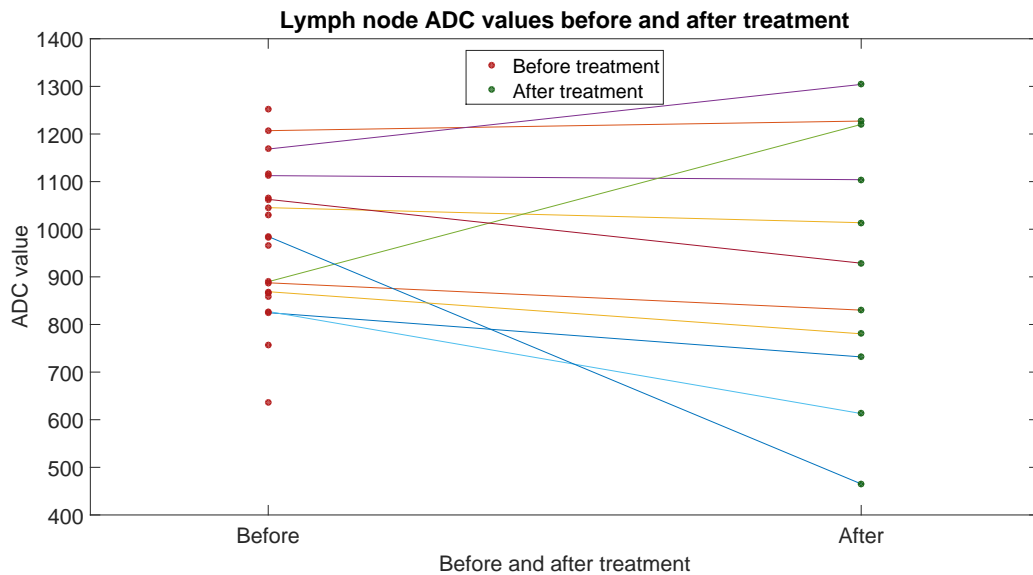


Figure 66: ADC values before and after treatment. Lines indicates changes in ADC values for lymph nodes that were present before and after treatment.

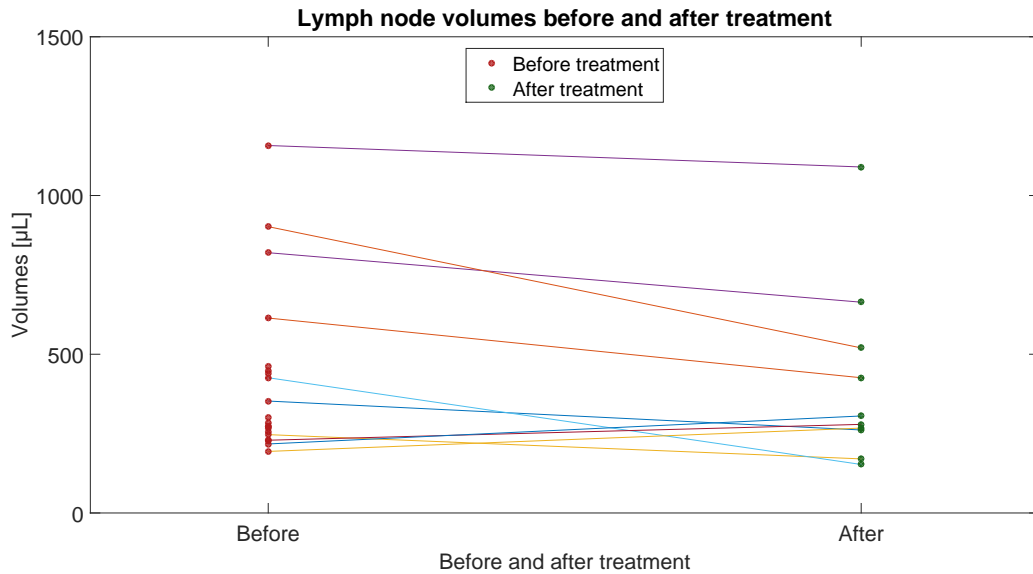


Figure 67: Lymph node volumes before and after treatment. Lines indicates changes in volumes for lymph nodes that were present before and after treatment. One lymph node with a volume of 3700 µL before and 5800 µL after treatment is not shown in the figure.

The total volume of all lymph nodes before chemoradiotherapy was 12.1 mL and the total volume of all lymph nodes available after chemoradiotherapy was 9.96 mL. The mean ADC value of all lymph nodes before treatment was  $972 \times 10^{-6} \text{ mm}^2 \text{ s}^{-1}$  and  $929 \times 10^{-6} \text{ mm}^2 \text{ s}^{-1}$  after treatment. The total number of lymph nodes segmented in the images before the chemoradiotherapy was 21 and the number of segmented lymph nodes after treatment was 11.

The mean change in ADC values of the lymph nodes that were present both before and after treatment was  $-60 \times 10^{-6} \text{ mm}^2 \text{ s}^{-1}$ , not significant at the 0.05 level ( $p = 0.28$ , Wilcoxon signed rank test). The mean change in volume of the lymph nodes that were present both before and after treatment was 96 µL, not significant at the 0.05 level ( $p = 0.28$ , Wilcoxon signed rank test).

One lymph node increased in volume from 3700 µL before treatment to 5800 µL after treatment. Swelling, oedema and inflammation were possible interpretations by radiologists. When this lymph node was treated as an outlier and excluded from the data, then the mean change in ADC values of the lymph nodes was  $-99 \times 10^{-6} \text{ mm}^2 \text{ s}^{-1}$ , not significant at the 0.05 level ( $p = 0.084$ ). The mean change in volume of the lymph nodes was  $-100 \text{ µL}$ , not significant at the 0.05 level ( $p = 0.065$ ).

An example of a lymph node segmented by the radiologists with the program is shown in figures 68–70. Note that the field of view and zoom factor differs between the figures.

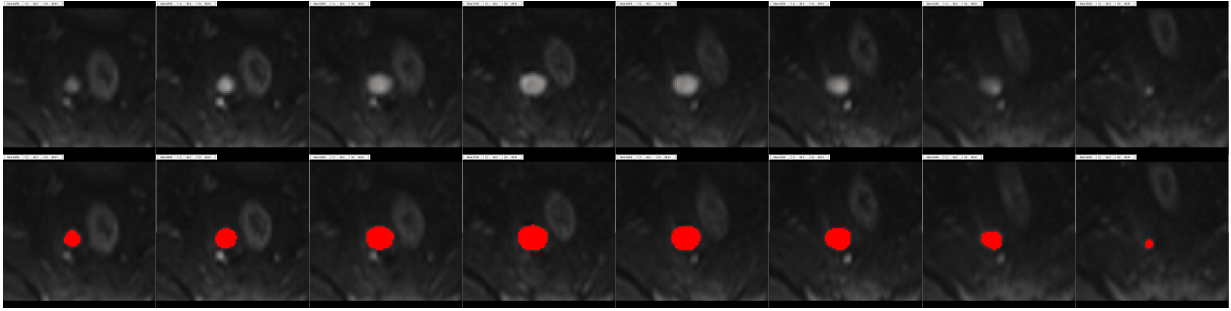


Figure 68: Transverse slices of a lymph node before chemoradiotherapy is shown in the upper row. The lower row shows the segmentation result.

The lymph node shown in figure 68 have a volume of 3750  $\mu\text{L}$  and a mean ADC value of  $890 \times 10^{-6} \text{ mm}^2 \text{ s}^{-1}$ .

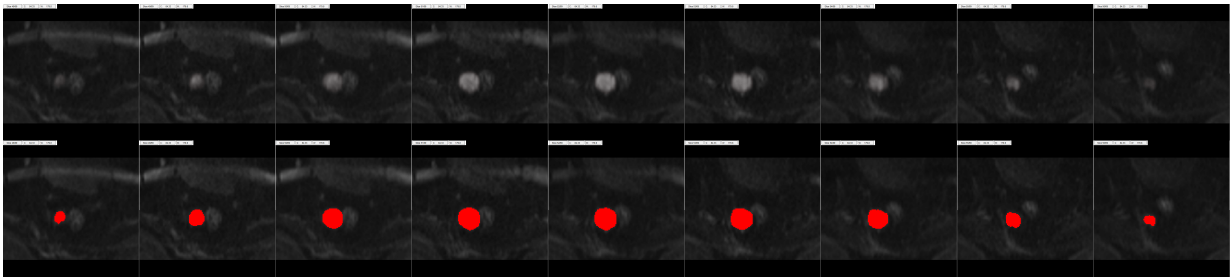


Figure 69: Transverse slices of a lymph node during chemoradiotherapy is shown in the upper row. The lower row shows the segmentation result.

The lymph node shown in figure 69 have a volume of 8410  $\mu\text{L}$  and a mean ADC value of  $1060 \times 10^{-6} \text{ mm}^2 \text{ s}^{-1}$ .

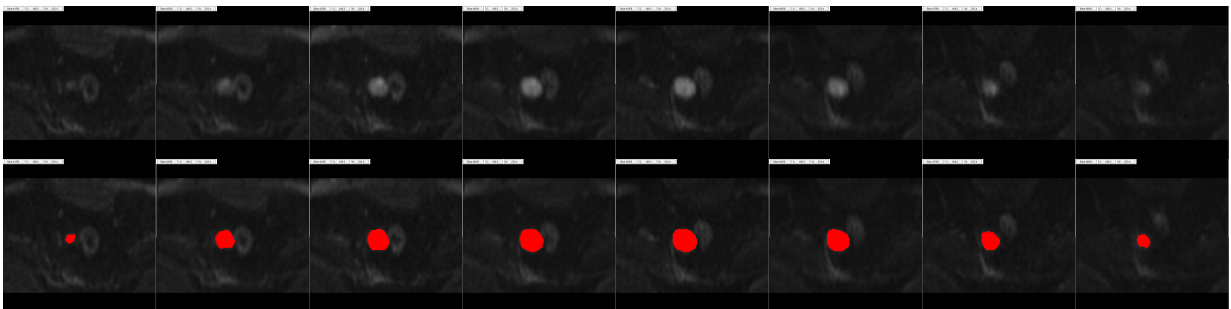


Figure 70: Transverse slices of a lymph node after chemoradiotherapy is shown in the upper row. The lower row shows the segmentation result.

The lymph node shown in figure 70 have a volume of 5820  $\mu\text{L}$  and a mean ADC value of  $1220 \times 10^{-6} \text{ mm}^2 \text{ s}^{-1}$ .

---

Histograms of the ADC values of the lymph node shown in figures 68–70 are shown in figures 71–73. Note that the skewness changes during the course of the treatment. Also note that these histograms may not represent a typical lymph node, since the lymph node they were calculated from was exceptionally large and had an increased mean ADC value after treatment, whereas a typical lymph node decreased in value. These histograms are shown due to the large number of voxels in this lymph node, which allows for a smaller histogram bin size which better visualizes the histogram. ADC values from several smaller lymph nodes with similar attributes and responses would have had to be combined to obtain an equally well visualized histogram for small lymph nodes.

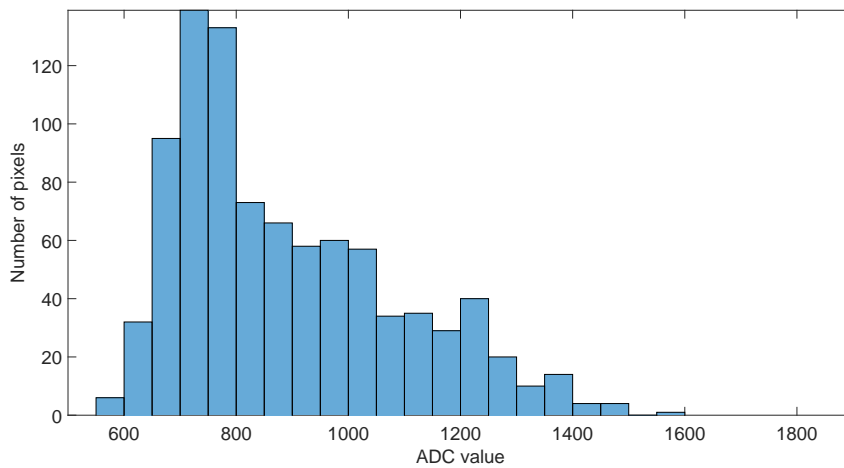


Figure 71: Histogram over the ADC values of a lymph node before chemoradiotherapy.

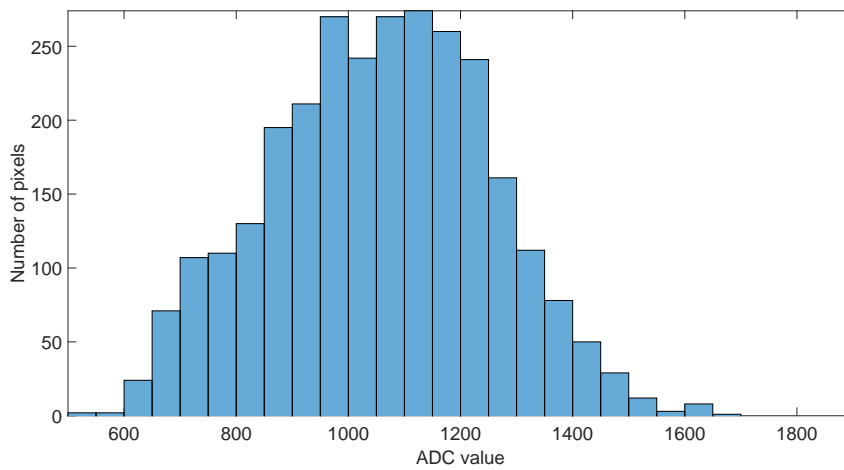


Figure 72: Histogram over the ADC values of a lymph node during chemoradiotherapy.

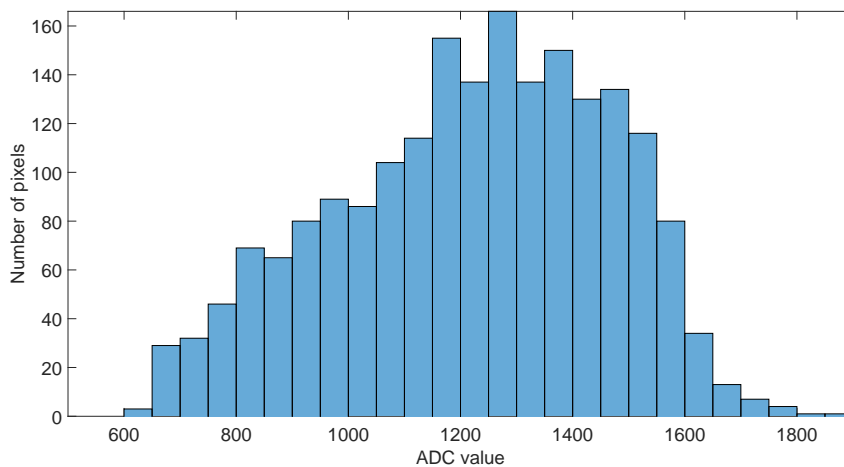


Figure 73: Histogram over the ADC values of a lymph node after chemoradiotherapy.

---

The program failed to segment lymph nodes in 3 instances.

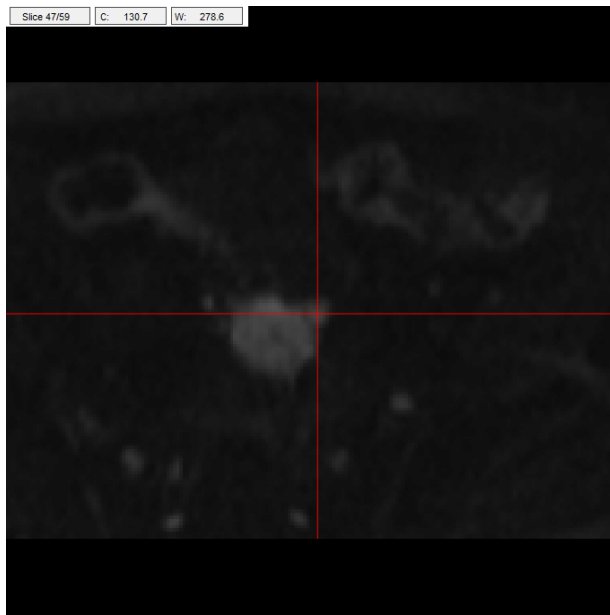


Figure 74: A lymph node that the algorithm failed to segment is indicated by the crosshair.



Figure 75: Segmented lymph node.

The segmentation of the object in figure 74 failed because the region growing algorithm used to locate the lymph node center leaked out into the primary tumour connected to the lymph node. The segmentation result when the lymph node center was marked manually is shown in figure 75. The segmented volume was considered too large by the radiologists. A similar problem was encountered for a lymph node in another patient that was also attached to a nearby structure.

The program also failed to segment one lymph node in close proximity to another lymph node shown in figure 76. One of the lymph nodes was successfully segmented, but the region growing algorithm leaked into the other lymph node during the segmentation of the second lymph node. This resulted in an origin for the 3D scanning algorithm located between the two lymph nodes which caused the algorithm to segment both nodes. This segmentation is shown in figure 77.

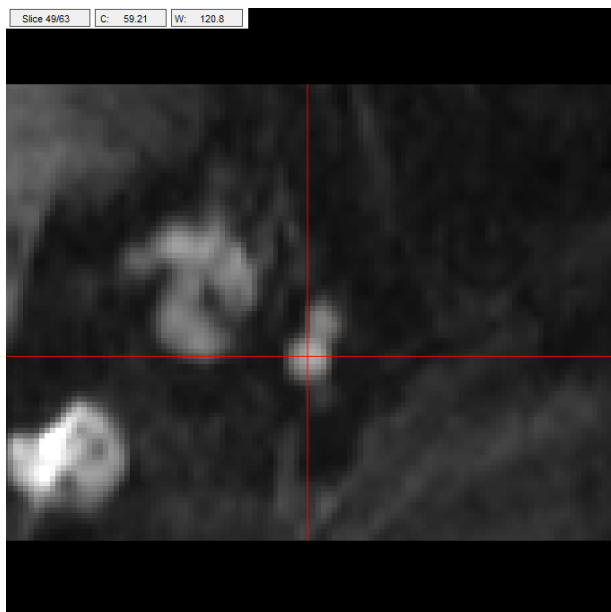


Figure 76: Two attached lymph nodes marked by the crosshair.



Figure 77: Segmentation of two lymph nodes.

---

## 6 Discussion

Several techniques were developed and/or evaluated for segmentation of lymph nodes in single diffusion weighted image slices in this work. The techniques had to be able to segment lymph nodes without the need for user to adjust the segmentation parameters, since a program with a segmentation technique with results independent of the user was desired in order to eliminate inter- and intra-observer variation in the segmentation result.

It was noted early that thresholding and region growing algorithms which only used pixel intensities for the segmentation objects didn't yield satisfactory results. Such methods often included nearby structures that the lymph node was attached to in the segmented region. To only use pixel intensities for segmentation was therefore considered insufficient. Several techniques using both pixel intensities and image gradients were therefore developed and evaluated to better separate lymph nodes from nearby objects. Region growing algorithms using pixel intensities and image gradients yielded satisfactory results and were considered possible candidates for further development and 3D segmentation.

The 2D scanning algorithm and the two associated definitions of external forces yielded satisfactory results on several lymph nodes. However the results were worse when the algorithms were tested on other objects such as nerves and other elongated objects. The reason for the difficulties with elongated objects is that such objects may have sharp outgrowths in the k-r-space image, as shown in figure 52. In order for the path to follow such sharp outgrowths, the spring constant  $k$  needs to be lowered considerably. However, lowering the spring constant makes each point on the path more independent from its neighbours and discontinuities in the path may occur where neighbouring points converges to different edges in the image. The algorithms are also unable to segment some objects with more complicated shapes, such as toroidal objects, since such objects require multiple points per radial line to delineate their surfaces. These drawbacks of the method are not a problem for the segmentation of lymph nodes, which are mostly spherical or ellipsoidal and not as elongated as nerves.

The expansion of the spiral scanning technique from 2 to 3 dimensions wasn't very extensive, since the segmentation of the object was still made in the 2D k-r-space. In the 2D technique, the number of radial lines required to delineate some objects were found to be around 100. This number of radial lines per revolution was kept in the 3D technique, which meant that  $10^4$  radial lines were used. This number wasn't changed since the time required to segment an object was reasonable, i.e. around 10-20 seconds.

The 3D scanning technique seemed to perform better than the 2D technique when tested on elongated object such as nerves. This could be due to minor changes in the weight factors or the spring constant, or possibly a result of the 3D technique seeing the whole objects in 3 dimensions while the 2D technique only uses axial slices. If a better segmentation of elongated objects is desired, then



---

the rotatable scanning axis for 3D spiral scanning algorithms introduced by Lei Wang et al. which improved the segmentation results when the scanning axis was aligned with the largest diameter of the lymph node [7], could be investigated. However, the 3D technique still have the drawback of the 2D technique of not being able to segment complicated shapes, such as toroidal objects.

The 3D scanning technique was able to segment most lymph nodes successfully. However, the radiologists impressions of the program after testing it on 4 patients were that it produced slightly too large VOIs. This could be corrected by adjusting the weight factors used by the external force. Alternatively, the first external force which used a potential energy based on the image gradient could be investigated further. This external force was removed in favour of the second external force because it was less reliable at completely locating lymph node surfaces and because the segmentation results were deemed less correct compared to the second external force. However, the potential energy based external force generally produced smaller regions in the 2D implementation compared to the second external force. The reason for this behaviour could be because the potential energy based external force attracts the path towards the steepest edges whereas the second external force tends to place the path at the beginning of an edge. An external force based on a linear combination of the two external forces could perhaps combine the reliability of locating edges from second external force with the steepest edge seeking ability of the first external force. This would however increase the number of weight factors that needs to be balanced against each other. An alternative method could be to initially use the second external force in the iterative algorithm to place the path near the edge of the lymph node and then change the external force to the potential energy based force to refine the segmentation result.

The 3D scanning technique used in this work used the sampling technique with an even partition of azimuth and elevation angles in a sequential order (figure 3(b)) instead of the sampling technique with the even spatial distribution of radial lines. This was chosen due to the ease of identifying neighbouring points in the latitude direction. However, having an even distribution of elevation angles is according to Wang, J et al. a disadvantage that yields a higher number of radial lines around the two poles than on the equator. The authors doesn't elaborate why this is a disadvantage, but they do report slightly worse segmentation results for the technique with the even partition of elevation angles compared to the technique with the even spatial distribution of radial lines. This result was measured as the mean overlap between the segmentation algorithm outputs and gold standards derived from outlines made by six expert chest radiologists and was 63 % for even partition of elevation angles and 66 % for even spatial distribution of radial lines. A possible disadvantage of the uneven spatial distribution of the radial lines in this work could be that two neighbouring points located close to each other near a pole are allowed by the internal force to vary in radial position as much as two neighbouring points near the equator that are located further away from each other. This means that the surface is allowed to have more sharp bumps near the poles than near the equator due to

---

neighbouring points being closer to each other spatially near the poles. A partial solution to this disadvantage could be to increase the spring force constant  $k$  and the internal force near the poles. Such a solution was not implemented however, since a more noisy or uneven surface near the poles was not observed and since varying values of  $k$  would potentially cause pairs of points to exert spring forces of different strengths on each other and thus not follow Newton's third law of equal and opposite forces. A perhaps better solution could be to use the even spatial distribution of radial lines instead and have the internal force consider the radial positions of all nearby points within a distance  $R$  when calculating the internal force on a point instead of considering neighbours only in the latitude and longitude directions. Another disadvantage would be that the higher amount of radial lines than necessary near the poles leads to a waste or unoptimal use of computing resources. A smaller amount of radial lines and thus a shorter total segmentation time, or a higher number of radial lines and thus a higher accuracy near the equator with unchanged segmentation time could have been obtained with an even spatial distribution of radial lines.

As shown in table 1, the multislice data used in this work had non isotropic resolutions with typical distances of approximately 2.3 mm between neighbouring pixel centres within a slice and 6 mm between slices. To minimize the influence of this data aspect ratio on the appearance of objects in the 2D k-r-space images obtained from the 3D spiral scanning algorithm, the sample points on the radial lines used coordinates in millimetres into the multislice data instead of coordinates in terms of array indices. This way, the surface of a spherical object would appear as a horizontal edge in the 2D image independently of the voxel aspect ratios used when imaging the object due to the surface radius being constant as a function of radial line number. If coordinates in terms of array indices had been used in the spiral scanning instead, then the contour of a spherical object would have appeared as a periodically oscillating edge as a function of the radial line number in the 2D k-r-space image due to the surface having a different radii in different directions when measured in array indices. For such an edge, the internal and external forces would work against each other unnecessarily with the external forces trying to have the line through the k-r-space image oscillating to follow the edge and the internal forces trying to have the line smooth and horizontal. Thus, by using coordinates in millimetres in the multislice data, this issue of internal and external forces working against each other unnecessarily was avoided.

Another possible issue with the non isotropic resolution was that the image gradients in the multislice data and the corresponding vertical gradients in the 2D k-r-space image could have appeared weaker in the slice selection direction than in the other directions when measured as the change in signal strength per mm, since the voxel depth was higher (6 mm per pixel) than the in-slice dimensions of the voxels (2.3 mm per pixel). This could have affected the segmentation results around the poles of the scanning patterns due to the possibly weaker image gradients there, but the normalization term per radial line  $g_{\max}(n)$  in equation 11 and 13, which corrects for weaker edge strengths in the

---

columns in the 2D k-r-space image should prevent this.

The non isotropic resolution of the multislice data should therefore not have any greater effect on the segmentation results as a result of these two measures, but this has not been verified against reference images of isotropic resolutions. A series measurements with different isotropic and non isotropic resolutions could be made with a magnetic resonance camera and a lymph node-like phantom in a future work to examine the effects, or lack of effects, of the image resolution and data aspect ratio on the segmentation results.

No quantitative comparison between manual segmentations and the segmentation techniques investigated in this work has been done, since no manual segmentation maps have been available. An overlap value between manual and semi-automatic segmentations would have been a valuable measurement for the evaluation of the segmentation techniques in the segmentation evaluation program and in the primary program. A program for manual segmentation of lymph nodes and the resulting segmentations of multiple radiologists would have been required for this to be possible. Such a program could have been developed if more time had been available.

The data obtained with the program indicated that lymph nodes tend to decrease in volume after chemoradiotherapy according to the radiologists. The mean change in volume was not significant, but some of the lymph nodes had become too small to be visible or measurable after the treatment according to the radiologists. The indication of a decrease in ADC values, although not statistically significant, was an unexpected result. A low ADC value is normally a sign of malignancy and a high ADC value indicates a benign lymph node. One theory is that the lymph nodes shrink and becomes hard lumps with lower ADC values during the treatment. The slightly too large VOIs may also have affected the ADC values, since voxels outside the lymph nodes may have been included when calculating the mean ADC values. This would mainly affect small lymph nodes.

Histograms of the ADC values of the lymph nodes may also be of interest for radiologists and a interface to display histograms was therefore developed. Histograms of the ADC values of a lymph node before, during and after chemoradiotherapy are shown in figures 71–73. It is the distribution and primarily its skewness that may be of interest. The peak and the skewness is shifted towards higher ADC values after the chemoradiotherapy for this lymph node, which follows the behaviour hypothesized by the radiologists, which expected the ADC values to shift towards the higher, benign values. The shifting of the skewness is an interesting finding, since it may show the lymph node becoming benign under the course of the treatment. The result from this lymph node was an exception which differed from most other lymph nodes which had decreased ADC values after the treatment. This lymph node was also exceptionally large. More tests are required to determine if such behaviours of the peak and skewness occur in smaller lymph nodes. These results are preliminary, since only four patients were evaluated.

---

The current tools available to the radiologists allow them to draw regions of interest in each image slice, which is mainly done in the DWI images. There is however currently no simple way to move a ROI from a DWI image to an ADC map. There is also no simple way to measure ADC values in a volume and only mean values can be measured. There is no method available to obtain histograms of the ADC values with the current tools. The primary program could be useful to radiologists by providing a simpler and faster way to segment lymph nodes in multislice images and transfer the VOIs to ADC maps, and by providing the ability to generate histograms. The program could also reduce or remove inter- and intra observer variability by replacing manual segmentation with a semi-automatic algorithm. However, these advantages requires the segmentation algorithm to satisfactory segment lymph nodes. The program would be less useful if the segmentation technique cannot segment lymph nodes sufficiently well. Further evaluation of the program and adjustment of weight factors for the external energy is required before definite conclusions about the primary program can be made. If the segmentation algorithm is found to fail in some circumstances or only work well in certain situations, then it could possibly be complemented with a tool to manually add and remove voxels from the VOIs. This could however reduce the user-independency of the segmentation results.

If more time to develop the primary program had been available, then alternative segmentation techniques which would require more time to implement, such as the dynamic programming based technique used by other 3D spiral scanning algorithms, could have been investigated. Alternatives to the internal spring force could also have been investigated, such as the internal energies used by active contour algorithms which use the first and second derivative of the contour boundary to control its smoothness.

---

## 7 Conclusions

Preliminary results indicated that the 3D spiral scanning algorithm was capable of segmenting lymph nodes in multislice diffusion weighted images of the abdomen, but further evaluations and verdicts from radiologists are required.

Data obtained by radiologists when testing the primary program indicated that lymph node volumes and ADC values decrease after chemoradiotherapy. The indication of a decrease in ADC values after treatment was contradictory to what was expected. The results were not statistically significant however and more patients are required to draw definite conclusions.

---

## 8 References

1. *Tjock- och ändtarmscancer*, Cancerfonden, retrieved 20 April 2015, <<https://www.cancerfonden.se/om-cancer/tjock-och-andtarmscancer>>.
2. Regionala cancercentrum 2008, *Kolorektal cancer Nationellt vårdprogram 2008*, Regionala cancercentrum, retrieved 27 April 2015, <[http://www.cancercentrum.se/PageFiles/2823/Kolorektal%20cancer%20nya\\_vardprogrammet\\_081120%20\(1\).pdf](http://www.cancercentrum.se/PageFiles/2823/Kolorektal%20cancer%20nya_vardprogrammet_081120%20(1).pdf)>.
3. Beets-Tan, RGH & Beets, GL 2004, 'Rectal Cancer: Review with Emphasis on MR Imaging', *Radiology*, Volume 232, Issue 2, pp. 335–346.
4. Brown, G, Richards, CJ, Bourne, MW, Newcombe, RG, Radcliffe, AG, Dallimore, NS & Williams, GT 2003, 'Morphologic Predictors of Lymph Node Status in Rectal Cancer with Use of High-Spatial-Resolution MR Imaging with Histopathologic Comparison', *Radiology*, Volume 227, Issue 2, pp. 371–377.
5. Koh, DM, Blackledge, M, Padhani, AR, Takahara, T, Kwee, TC, Leach, MO & Collins, DJ 2012, 'Whole-Body Diffusion-Weighted MRI: Tips, Tricks, and Pitfalls', *American Journal of Roentgenology*, Volume 199, Issue 2, pp. 252–262.
6. Yu, SP, He, L, Liu, B, Zhuang, XZ, Liu MJ & Hu, XS 2010, 'Differential diagnosis of metastasis from non-metastatic lymph nodes in cervical cancers: pilot study of diffusion weighted imaging with background suppression at 3T magnetic resonance', *Chinese Medical Journal*, Volume 123, Issue 20, pp. 2820–2824.
7. Wang, L, Moltz, J H, Bornemann, L & Hahn, H K 2012, 'A Minimally-interactive Method to Segment Enlarged Lymph Nodes in 3D Thoracic CT Images Using a Rotatable Spiral-Scanning Technique', in B Ginneken & C L Novak (eds), *Proceedings of SPIE 8315, Medical Imaging 2012: Computer-Aided Diagnosis*, SPIE, San Diego, California, USA, doi:10.1117/12.912935.
8. Smeets, D, Loeckx, D, Stijnen, B, De Dobbelaer, B, Vandermeulen, D & Suetens, P 2010, 'Semi-automatic level set segmentation of liver tumors combining a spiral-scanning technique with supervised fuzzy pixel classification', *Medical Image Analysis*, Volume 14, pp. 13–20.
9. Wang, J, Li, Q, Hirai, T, Katsuragawa, S, Li, F & Doi, K 2008, 'An Accurate Segmentation Method for Volumetry of Brain Tumor in 3D MRI', in J M Reinhardt & J P W Pluim (eds) *Proceedings of SPIE 6914, Medical Imaging 2008: Image Processing*, SPIE, San Diego, California, USA, doi:10.1117/12.771480.
10. Wang, J, Engelmann, R, & Li, Q 2007, 'Segmentation of pulmonary nodules in three-dimensional CT images by use of a spiral-scanning technique', *Medical Physics*, Volume 34, pp. 4678–4689.

- 
11. Bankman, I N 2000, *Handbook of Medical Imaging*, Academic Press, doi:10.1016/B978-0-12-077790-7.50064-3.
  12. Zhou, W & Xie, Y 2013, 'Interactive Medical Image Segmentation Using Snake and Multiscale Curve Editing', *Computational and Mathematical Methods in Medicine*, Volume 2013, pp. 1–13.
  13. Jiang, L, Lian, Y, Gu, Y & Li, Q 2013, 'Breast segmentation in MR images using three-dimensional spiral scanning and dynamic programming', in C L Novak & S Aylward (eds), *Proceedings of SPIE 8670, Medical Imaging 2013: Computer-Aided Diagnosis*, SPIE, Lake Buena Vista (Orlando Area), Florida, USA, doi:10.1117/12.2008129.
  14. Kass, M, Witkin, A, & Terzopoulos, D 1988, 'Snakes: Active Contour Models', *International Journal of Computer Vision*, Volume 1, Issue 4, pp. 321–331.
  15. Sethian, J.A 1996, 'A fast marching level set method for monotonically advancing fronts', *Proceedings of the National Academy of Sciences of the United States of America*, Volume 93, Issue 4, pp. 1591–1595.
  16. Sethian, J.A 1999, 'Fast Marching Methods', *Society for Industrial and Applied Mathematics Review*, Volume 41, Issue 2, pp. 199–235.
  17. Sethian, J.A c. 2006, *Fast Marching Methods: A boundary value formulation*, University of California, Berkeley, retrieved 7 May 2015, <[https://math.berkeley.edu/~sethian/2006/Explanations/fast\\_marching\\_explain.html](https://math.berkeley.edu/~sethian/2006/Explanations/fast_marching_explain.html)>.